PHYSICAL REVIEW B **95**, 045102 (2017)

Floquet engineering of Haldane Chern insulators and chiral bosonic phase transitions

Kirill Plekhanov,[1,2] Guillaume Roux,[1] and Karyn Le Hur[2]
[1]*LPTMS, CNRS, Univ. Paris-Sud, Université Paris-Saclay, F-91405 Orsay, France*
[2]*Centre de Physique Théorique, Ecole Polytechnique, CNRS, Université Paris-Saclay, F-91128 Palaiseau, France*

(Received 15 August 2016; revised manuscript received 27 November 2016; published 3 January 2017)

The realization of synthetic gauge fields has attracted a lot of attention recently in relation to periodically driven systems and the Floquet theory. In ultracold atom systems in optical lattices and photonic networks, this allows one to simulate exotic phases of matter such as quantum Hall phases, anomalous quantum Hall phases, and analogs of topological insulators. In this paper, we apply the Floquet theory to engineer anisotropic Haldane models on the honeycomb lattice and two-leg ladder systems. We show that these anisotropic Haldane models still possess a topologically nontrivial band structure associated with chiral edge modes. Focusing on (interacting) boson systems in s-wave bands of the lattice, we show how to engineer through the Floquet theory, a quantum phase transition (QPT) between a uniform superfluid and a Bose-Einstein condensate analog of Fulde-Ferrell-Larkin-Ovchinnikov states, where bosons condense at nonzero wave vectors. We perform a Ginzburg-Landau analysis of the QPT on the graphene lattice, and compute observables such as chiral currents and the momentum distribution. The results are supported by exact diagonalization calculations and compared with those of the isotropic situation. The validity of high-frequency expansion in the Floquet theory is also tested using time-dependent simulations for various parameters of the model. Last, we show that the anisotropic choice for the effective vector potential allows a bosonization approach in equivalent ladder (strip) geometries.

DOI: 10.1103/PhysRevB.95.045102

I. INTRODUCTION

A. Generalities and experimental context

Topological phases of matter play an important role, from quantum Hall physics [1–3] to the concept of symmetry protected topological phases [4–8]. Topological Bloch bands have also been detected in quantum materials (topological insulators) [9–14], ultracold atoms [15–17], and photon systems [18–21]. Very recently, experimental realizations of the Harper-Hofstadter model [22,23] were performed with ultracold atoms by using the laser-assisted tunneling technique [24–27], proposed for the first time in Ref. [28]. At the same time, the possibility of generating artificial gauge fields was transferred into the domain of electromagnetic waves, giving opportunity to realize photonic chiral edge modes associated with Bloch bands with nonzero Chern numbers [29,30]. Several years later, such objects were realized experimentally using the lattice of ferrite rods [31] and in a system of coupled optical-ring resonators [32]. In a similar way, the artificial magnetic field realization of the effective Haldane model [33], known as the model for the quantum anomalous Hall effect, was done first by using the array of evanescently coupled helical waveguides with the propagation coordinate z playing the role of time [34], and later in the system of shaken honeycomb optical lattice [35], following the first experimental realization of artificial graphene with ultracold atoms [36,37]. This occurred in parallel to first observations of the quantum anomalous Hall effect in quantum materials [38] (an overview on recent progress in this domain can be found in Refs. [39,40]). Recent experimental realization of Floquet engineered bands in tunable honeycomb lattices with full momentum-resolved measurement of the Berry curvature was also reported in Ref. [41].

From a complementary point of view, in the case of bosonic ultracold atoms systems (or also exotic polariton superfluids [42] and photonic BECs [43]), the realization of the Haldane model as reported in Refs. [35,41] allows one to investigate the rich properties of lattice bosons subjected to artificial gauge fields. Such studies were performed in one dimension [44,45] and ladder [46] systems, on triangular [47,48] and square [49] lattices. It is known that this can give rise to the condensation of bosons at nonzero momentum [50–53]—the effect showing similarity to the FFLO phase [54,55]. Finite momentum BEC was also predicted [56–58] and observed [59,60] with p-wave band superfluids and for a near-resonant hybridization of s and p bands of bosons [61,62].

Importantly, experimental realizations of artificial magnetic fields in ultracold atom systems and in photonic lattices are based on the application of a periodic time-dependent perturbation. In the case of a nonresonant coupling, the Floquet theory is often used to solve the problem. According to the Floquet theory [63–65], one expects that the dynamics of such systems in the high-frequency regime will be separated into the “slow” and “fast” parts. The slow dynamics will thus be simply described in terms of a time-independent effective (Floquet) Hamiltonian. Generally, an exact expression of the effective (Floquet) Hamiltonian is not accessible and one should rely on approximations such as, for example, the Magnus expansion [66,67] or the HFE (high-frequency expansion) [68–72] (see Refs. [73–75] for general review and comparison of the two approaches). These expansions are perturbative and their convergence is not ensured even in the relatively simple case of noninteracting systems. When interactions must be taken into account, the situation becomes even more complicated. The behavior of driven many-body systems was studied theoretically and numerically [76–89] and the invalidity of the HFE was often related to the problem of heating in many-body systems [80–95].

Nevertheless, today a lot of interest is dedicated to “Floquet engineering” [73–75,96]. More generally, it consists of generating an effective (Floquet) Hamiltonian with desired properties, starting from a more trivial one by superimposing a periodic time-dependent perturbation. Using the Floquet theory (and the high-frequency expansion) and a well-chosen geometry allows one to design targeted Hamiltonians. Many theoretical studies were done in order to investigate the possibility of obtaining Floquet topological (Chern) insulators from irradiated graphene structures [97–106] that were recently observed experimentally [107]. Driven superconducting systems were considered in order to observe Floquet Majorana fermions [108–113]. These works are in deep connection with the study of topological properties and corresponding topological invariants of periodically driven systems [114–122], showing that their topological structure is even richer then in the general classification at equilibrium [123].

B. Aims and structure of the paper

In the present work, our first goal is to investigate the possibility of observing photonic analogs of Bloch bands with nonvanishing Chern numbers and related edge modes, that are topologically protected from scattering. In this context, we propose a way to engineer an anisotropic version of the Haldane model [33]. Our starting point is the nonequilibrium system that was theoretically proposed in Refs. [124,125] and recently realized experimentally, as reported in Ref. [126]. The considered system and related experimental realizations are discussed in Sec. II. This discussion is followed by precise calculations of the effective Hamiltonian and the effective evolution of the system, based on the application of the Floquet theory [63–65] and the HFE [68–75]. In Sec. III A we show that the effective Hamiltonian corresponds to the anisotropic Haldane model. We verify that topological properties of the Haldane model subsist in the anisotropic case and determine the related topological phase transition in Sec. III B.

Secondly, in Sec. IV we show that the configuration of artificial magnetic fields, appearing in the effective anisotropic Haldane model described in the current work and considered also in Ref. [35], supports the finite momentum phase with a two-well structure for the ground state of bosons in s-wave bands. The transition between the zero momentum (described in Secs. IV A and IV B) and the finite momentum phase (Secs. IV C and IV D) is of second order, in contrast to the isotropic situation where chiral currents show a discontinuity at the phase transition [53]. Observables such as chiral currents and momentum distribution are studied and the role of moderate interactions on the QPT is discussed in Sec. IV E. Then, in Sec. V we check the validity of the HFE by performing numerical comparison of the time evolution with exact and effective Hamiltonians and we infer the regime of consistency between the two Hamiltonians, in which above mentioned properties of the system should be accessible for the experimental observation.

Finally, in Sec. VI we study a ladder analog of the anisotropic Haldane model. The nature of the QPT between the zero momentum and the finite momentum phase changes, giving rise to the apparition of flat bands (Sec. VI A). The role of interactions far from the flat band region is then studied using bosonization [127–130] (Secs. VI B–VI D). This ladder version of the model is similar to the current experimental development in ultracold atoms system reported in Ref. [46]. We also mention some other ladder models that can be generated with the described approach on different types of lattices in Sec. VI E.

Extra technical details will be provided in the appendixes. Appendix A will discuss the Floquet theory and the Dyson expansion to compute observables. In Appendix B, we discuss in more detail the Ginzburg-Landau expansion in the finite-momentum (FM) phase in the presence of interactions.

II. TIME-DEPENDENT MODEL

The system is described by the Hamiltonian $\hat{H}(t) = \hat{H}_0 + \hat{V}(t)$, defined on a bipartite lattice where the two sublattices are denoted by A and B. The Planck constant $\hbar$ is set to unity for simplicity. The two terms read

$$\begin{aligned}\hat{H}_0 &= \omega_A \sum_{i\in A} \hat{a}_i^\dagger \hat{a}_i + \omega_B \sum_{j\in B} \hat{b}_j^\dagger \hat{b}_j - t_1 \sum_{\langle ij\rangle} (\hat{a}_i^\dagger \hat{b}_j + \hat{b}_j^\dagger \hat{a}_i),\\ \hat{V}(t) &= V \sum_{\langle ij\rangle} \cos(\omega t + \theta_{ij})(\hat{a}_i^\dagger \hat{b}_j + \hat{b}_j^\dagger \hat{a}_i). \qquad (1)\end{aligned}$$

Here $\hat{a}_i(\hat{b}_j)$ are annihilation operators on site $i(j)$ of sublattice $A(B)$, and $\omega_A(\omega_B)$ is the corresponding frequency in the case of a photonic optical lattice.

Sublattices are coupled through a constant tunneling term t_1 and a time-dependent term V (which is periodic in time with period $T = 2\pi/\omega$) coupling nearest neighbors. In cavity systems, this consists of coupling the cavities with dc and ac terms and assuming that each of them has approximately the same length. $\theta_{ij} = -\theta_{ji}$ are scalar phases associated with each oriented link between sites i and j, and $\sum_{\langle ij\rangle}$ denotes the summation over all possible pairs of nearest neighbors (NN) with i belonging to sublattice A and j to sublattice B. Related scenarios have been suggested to realize quantum Hall phases of bosons [131].

The laboratory frame realization of such a Hamiltonian was proposed in the context of photonic lattices [124,125]. It was also successfully implemented using superconducting qubits arranged in a triangular loop with pairwise couplings [126], based on earlier theoretical suggestions [132]. In the following sections we will show that this approach can be used to generate a photonic Chern insulator.

Similar systems were also experimentally realized with ultracold atoms, by using lattice shaking [35] or laser-assisted tunneling techniques [25–27]. Related theoretical proposals were considered in Refs. [28,133] and the photon-assisted tunneling was also suggested in Ref. [134]. In these cases we should, however, think of ω_A and ω_B as of chemical potentials on two sublattices, which have an additional periodic time-dependent component, whereas the hopping term is constant. It was argued that after moving to the rotating frame (and applying the Floquet theory in the nonresonant case), one can eventually generate artificial magnetic fields. In Ref. [35] this approach was used to effectively generate the anisotropic Haldane model. Within these protocols, we will show that we can engineer a BEC analog of FFLO states, where bosons (in the s-wave band of the optical lattice) condense at a nonzero wave vector.

Inspired by previous works [50,53], we are also interested in rich properties of the many-body system in the interacting regime. We consider the simplest possible case of interactions, described by the Hamiltonian term,

$$\hat{H}_{\mathrm{BH}} = \frac{U}{2} \sum_{i \in A \oplus B} \hat{n}_i(\hat{n}_i - 1), \tag{2}$$

where U is the strength of repulsive on-site Bose-Hubbard interactions and $\hat{n}_i$ is the number operator on site i. In the system of single-component bosons such interactions can originate from the s-wave collisions between atoms. An experimental realization of the Bose-Hubbard model can also be achieved in photonic lattices using nonlinear LC resonators (qubits) [126] or in the highly detuned limit, with an (approximately exact) mapping between the Jaynes-Cummings lattice model and the Bose-Hubbard model [135,136].

III. FLOQUET THEORY AND EFFECTIVE ANISOTROPIC HALDANE MODEL

In this section we determine properties of the system that evolves with the Hamiltonian $\hat{H}(t)$ of Eq. (1). We aim to engineer an effective system that can support edge modes topologically protected from scattering. Our approach is based on Floquet theory [63–65] and the related high frequency expansion (HFE) [69–75]. One can show that in the regime of high frequency ω, the "slow" long-time dynamics of the system can be described by a static effective Hamiltonian $\hat{H}_{\mathrm{eff}}$. A common approximation consists then of expressing the effective Hamiltonian in powers of $1/\omega$, in such a way that $\hat{H}_{\mathrm{eff}} = \sum_j \hat{H}^{(j)}_{\mathrm{eff}}$. Here we denote by $\hat{H}^{(j)}_{\mathrm{eff}}$ the contribution to $\hat{H}_{\mathrm{eff}}$ at the order j. Up to the first order, $\hat{H}_{\mathrm{eff}}$ has the following form [71–75]:

$$\hat{H}_{\mathrm{eff}} = \hat{H}^{(0)} + \frac{1}{\omega} \sum_{i=1}^{\infty} \frac{1}{i} [\hat{H}^{(i)}, \hat{H}^{(-i)}] + \cdots, \tag{3}$$

where $\hat{H}^{(i)}$ are distinct Fourier components of $\hat{H}(t)$. In this section we consider only the first-order contribution. The validity of such approximation is studied in Sec. V where we show that the effect of higher orders is irrelevant if ω is much larger than any other energy scale and the perturbation amplitude V behaves as $\sqrt{\omega t_1}$.

A. Generating effective anisotropic Haldane model

We apply the expansion of Eq. (3) to a system described by Eq. (1). The zero-order contribution reads $\hat{H}^{(0)}_{\mathrm{eff}} = \hat{H}_0$. At order one, we obtain

$$\begin{aligned}\hat{H}^{(1)}_{\mathrm{eff}} = {} & \frac{iV^2}{2\omega} \sum_{\langle\langle ik \rangle\rangle} \sin(\Theta_{ik})(\hat{a}^\dagger_i \hat{a}_k - \hat{a}^\dagger_k \hat{a}_i) \\ & - \frac{iV^2}{2\omega} \sum_{\langle\langle jl \rangle\rangle} \sin(\Theta_{jl})(\hat{b}^\dagger_j \hat{b}_l - \hat{b}^\dagger_l \hat{b}_j).\end{aligned} \tag{4}$$

We have defined $\Theta_{ik} = \theta_{ij} + \theta_{jk}$ for each couple of next-nearest neighbors (NNN) i and k sharing both the same NN with the index j. We have denoted by $\sum_{\langle\langle ik \rangle\rangle}$ the summation over all NNN on either sublattice A or sublattice B.

We see that terms in $\hat{H}^{(1)}_{\mathrm{eff}}$ are purely imaginary NNN hoppings whose amplitude $t_{2,ik}$ depends on the phases θ_{ij} and θ_{jk} on corresponding links:

$$t_{2,ik} = -\frac{V^2}{2\omega} \sin(\Theta_{ik}). \tag{5}$$

The physical interpretation of this effect can be seen as follows: When the hopping mediated by the time-driving term is performed, the particle acquires an energy ω. Since this energy is huge, the corresponding state is highly unstable and the particle is forced to perform the conjugated NN hopping and re-emits the energy ω. Since these hoppings are dephased in our model, this leads to the apparition of the effective phase acquired by the particle, resulting in the generation of an artificial gauge field.

In order to be able to solve the problem, one should consider a particular choice of the lattice geometry and of the phases θ_{ij}. By having in mind the idea of obtaining a topologically nontrivial model with nonzero Chern number, we decided to explore the possibility of generating an effective Haldane model [33]. We thus consider the problem defined on the honeycomb lattice from now on. Figure 1(a) represents a possible choice of phases θ_{ij} that fulfills our requirement. The resulting term in the effective Hamiltonian corresponds to the anisotropic Haldane model with absent horizontal NNN hoppings and with amplitude $t_2 = -V^2/2\omega$ of four leftover NNN hoppings at each unit cell:

$$\hat{H}^{(1)}_{\mathrm{eff}} = -t_2 \left(\sum_{\langle\langle ik \rangle\rangle}^{\mathrm{anis}} e^{\pm i\pi/2} \hat{a}^\dagger_i \hat{a}_k + \sum_{\langle\langle jl \rangle\rangle}^{\mathrm{anis}} e^{\pm i\pi/2} \hat{b}^\dagger_j \hat{b}_l + \mathrm{H.c.} \right). \tag{6}$$

In the last equation, we denoted the presence of the anisotropy by the label *anis* above the summation sign. The configuration of hopping amplitudes in the anisotropic model is also displayed in Fig. 1(b). The total magnetic flux through the unit cell of the lattice sums up to zero, such that Landau levels do not appear in the problem. We outline that phases θ_{ij} modify only the value of NNN hopping amplitudes and have no effect on the Haldane phase, which is always equal to $\pi/2$.

For the purpose of clarifying connections of the HFE to the standard perturbation theory, we perform calculations of some relevant observables (i.e., currents) by using Dyson series [137]. We deduce that results of both theoretical approaches coincide in the regime of weak time-dependent perturbation. Details of the calculations can be found in Appendix A. The validity of considering only the first-order term in the HFE will also be discussed in Sec. V.

B. Topological phase transition and chiral edge states

The Haldane model was first introduced as the model for the quantum anomalous Hall effect for noninteracting fermions at half-filling. In this section we want to show that the same characterization applies to the anisotropic Haldane model, which belongs to the class of Chern insulators and supports topologically protected edge modes. We emphasize that even very weak imaginary NNN hopping amplitude ($t_2 \ll t_1$) will be sufficient to observe edge states.

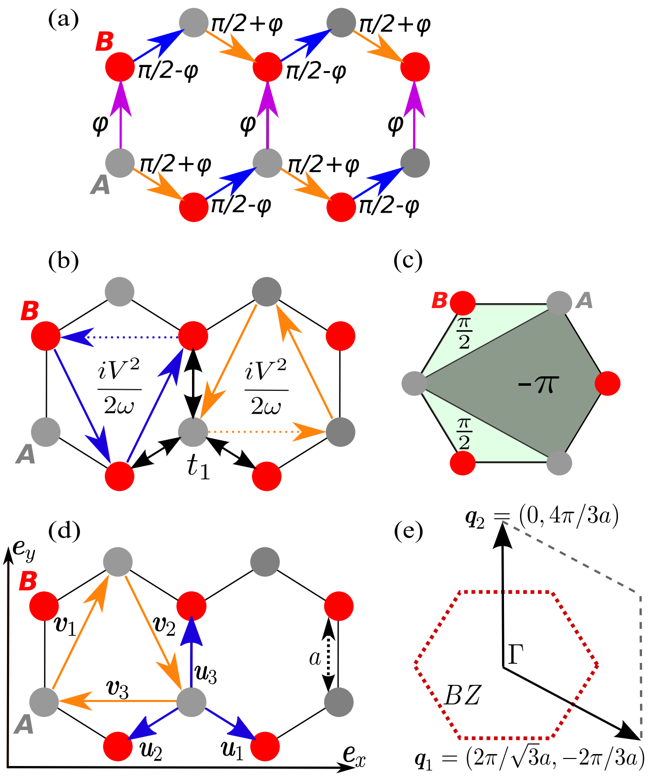

FIG. 1. (a) Distribution of phases on the NN bonds in the time-dependent Hamiltonian (1) required to generate effective anisotropic Haldane model. The phase φ is the free parameter. We notice that these phases only change the value of the NNN hopping amplitude and has no effect on the Haldane phase, that is always equal to $\pi/2$. (b) Anisotropic Haldane model. Colored bold lines represent NNN hoppings with amplitude modulus $\frac{V^2}{2\omega}$ and assigning a phase $\pm\pi/2$ if they are made in the anticlockwise (clockwise) direction. Dotted lines correspond to the hopping absent in the model. (c) Magnetic flux distribution in the anisotropic Haldane model. The total magnetic flux through the unit cell sums up to zero, with closed loops of vector potentials involving kite geometries rather then triangles as in the isotropic case. (d) Definition of vectors $\boldsymbol{u}_i$ and $\boldsymbol{v}_i$ on the honeycomb lattice. Each hexagon has the length of the side equal to a. (e) Reciprocal lattice vectors $\boldsymbol{q}_1$, $\boldsymbol{q}_2$ and the first Brillouin zone (BZ).

First, we fix the notation related to the structure of the Bravais lattice and reciprocal lattice. We define by $\boldsymbol{u}_i$, $i \in [1,2,3]$ vectors connecting each site on the sublattice A to its three first neighbors on the sublattice B. Then, $\boldsymbol{v}_k = \frac{1}{2}\sum_{i,j}\xi_{ijk}(\boldsymbol{u}_i - \boldsymbol{u}_j)$ (with ξ_{ijk}—the Levi-Civita symbol) are vectors connecting NNN sites on the same sublattices, as shown in Fig. 1(d). We also consider that the length of the side of each hexagon equals to a. We notice that any two vectors $\boldsymbol{v}_k$ form the basis of the Bravais lattice, that is given by one of sublattices A or B.

We remark then that the Hamiltonian $\hat{H} = \hat{H}_0 + \hat{H}^{(1)}_{\text{eff}}$ is easily diagonalized by going to momentum space:

$$\hat{a}(\hat{b})_{\boldsymbol{k}} = \frac{1}{\sqrt{N_c}}\sum_{i\in A(B)} e^{-i\boldsymbol{k}\cdot\boldsymbol{r}_i}\hat{a}(\hat{b})_i. \tag{7}$$

N_c is the number of unitary cells in the lattice and $\boldsymbol{k}$ is the momentum in the first Brillouin zone (BZ), which is spanned by vectors $\boldsymbol{q}_1 = (2\pi/\sqrt{3}a, -2\pi/3a)$ and $\boldsymbol{q}_2 = (0, 4\pi/3a)$ as depicted in Fig. 1(e). The Hamiltonian is then rewritten as

$$\begin{aligned}\hat{H} &= \sum_{\boldsymbol{k}\in\mathcal{BZ}} \hat{\psi}^\dagger_{\boldsymbol{k}} \cdot \mathcal{H}(\boldsymbol{k}) \cdot \hat{\psi}_{\boldsymbol{k}} \\ &= \sum_{\boldsymbol{k}\in\mathcal{BZ}} \hat{\psi}^\dagger_{\boldsymbol{k}} \cdot [\epsilon_0 I_{2\times 2} - \boldsymbol{d}(\boldsymbol{k})\cdot\boldsymbol{\sigma}] \cdot \hat{\psi}_{\boldsymbol{k}},\end{aligned} \tag{8}$$

where σ_j are Pauli matrices and $\epsilon_0 = (\omega_A + \omega_B)/2$. We have also defined the spinor $\hat{\psi}_{\boldsymbol{k}} = \binom{\hat{a}_{\boldsymbol{k}}}{\hat{b}_{\boldsymbol{k}}}$ and three functions of the momentum $\boldsymbol{k}$:

$$d_x(\boldsymbol{k}) = t_1 \sum_{i=1}^{3} \cos(\boldsymbol{k}\cdot\boldsymbol{u}_i),$$

$$d_y(\boldsymbol{k}) = t_1 \sum_{i=1}^{3} \sin(\boldsymbol{k}\cdot\boldsymbol{u}_i), \tag{9}$$

$$d_z(\boldsymbol{k}) = -M + 2t_2 \sum_{i=1}^{2} \sin(\boldsymbol{k}\cdot\boldsymbol{v}_i), \tag{10}$$

with $\boldsymbol{u}_i$ and $\boldsymbol{v}_i$ the vectors between NN and NNN sites, respectively, such that $\boldsymbol{v}_k = \frac{1}{2}\sum_{i,j}\xi_{ijk}(\boldsymbol{u}_i - \boldsymbol{u}_j)$ with ξ_{ijk} the Levi-Civita symbol, and $M = (\omega_A - \omega_B)/2$ is the Semenoff mass [138]. The eigenvalues of $\mathcal{H}(\boldsymbol{k})$ read

$$\begin{aligned}\epsilon(\boldsymbol{k}) &= \epsilon_0 \pm |\boldsymbol{d}(\boldsymbol{k})| \\ &= \epsilon_0 \pm \sqrt{d_x^2(\boldsymbol{k}) + d_y^2(\boldsymbol{k}) + d_z^2(\boldsymbol{k})}.\end{aligned} \tag{11}$$

The corresponding band structure is illustrated in Fig. 2 for various t_2 and M.

In order to study topological properties of this band structure, we take the expression of the Berry curvature $B(\boldsymbol{k})$ of an energy band:

$$B(\boldsymbol{k}) = \frac{\hat{\boldsymbol{d}}}{2}\cdot\left(\frac{\partial\hat{\boldsymbol{d}}}{\partial k_x}\times\frac{\partial\hat{\boldsymbol{d}}}{\partial k_y}\right) \quad \text{with } \hat{\boldsymbol{d}} = \frac{\boldsymbol{d}(\boldsymbol{k})}{|\boldsymbol{d}(\boldsymbol{k})|}. \tag{12}$$

The flux of the Berry curvature through the BZ is called the Chern number:

$$C_n = \frac{1}{2\pi}\int_{BZ} d^2\boldsymbol{k}\; B(\boldsymbol{k}). \tag{13}$$

This quantity expresses how the eigenfunction spinor wraps around the boundary of the BZ. Similarly to the isotropic Haldane model, a continuous gauge cannot be defined over the whole BZ, meaning that spinors possess singularities. It occurs at two Dirac points $\boldsymbol{K}_A$ and $\boldsymbol{K}_B$. Encircling only these points gives the possibility of estimating the Chern number. We find that the contribution at each point is equal to $\pm 1/2$, where the sign corresponds to the sign of $d_z(\boldsymbol{k})$.

The missing link does not affect the possibility of topological bands in the anisotropic Haldane model (thanks to the presence of closed loops of vector potentials involving kite geometries), but modifies the critical point of the topological versus nontopological phase transition and the edge-mode dispersion relation. More precisely, in the anisotropic Haldane

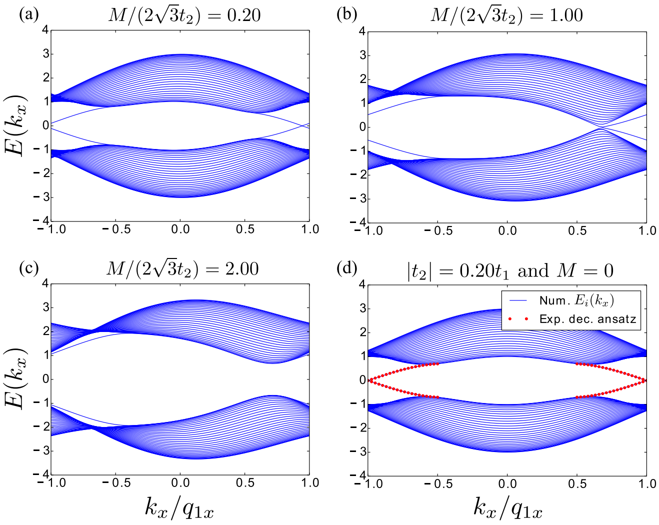

FIG. 2. (a)–(c) Numerical calculations of the band structure for the anisotropic Haldane model in the strip geometry with zigzag edges [cut along the x axis of Fig. 1(c)], showing the topological phase transition. Edge modes cross the gap between two bands for $M/t_2 < 2\sqrt{3}$. The gap closes at $M/t_2 = 2\sqrt{3}$. Edge modes do not cross the gap anymore for $M/t_2 > 2\sqrt{3}$. (d) Comparison between numerical results (solid blue lines) and analytical solution for edge modes based on an exponentially decaying ansatz [139,140] (red dotted lines). Band structure represented in this way is periodic with period $2q_{1x}$, where $\boldsymbol{q}_1$ is the reciprocal lattice vector defined in Fig. 1(d).

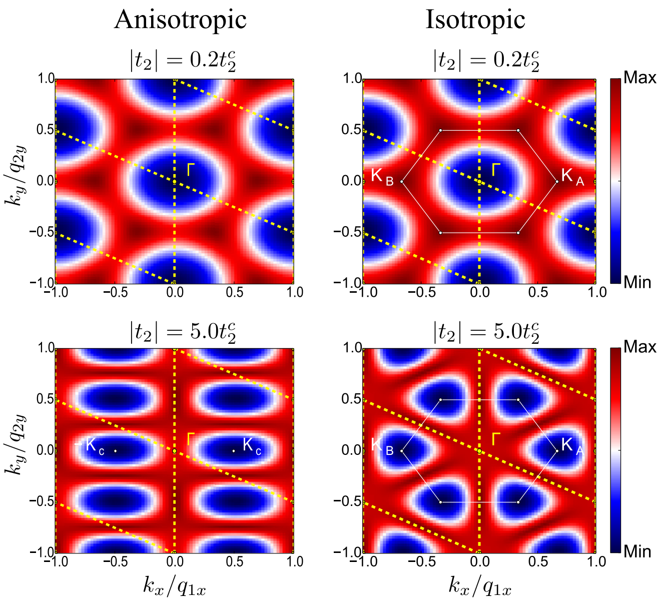

FIG. 3. Lowest energy band of the anisotropic Haldane model (on the left) and of the isotropic Haldane model (on the right) in the noninteracting case ($U = 0$), plotted for different values of t_2 (different lines). Here t_2^c is the "critical" value of the coupling when minima move away from the point $\boldsymbol{\Gamma}$. Yellow dotted lines represent reciprocal lattice generated by vectors $\boldsymbol{q}_1$ and $\boldsymbol{q}_2$ defined in Fig. 1(d). Presence of artificial gauge fields (complex NNN hoppings in our case) is required for observation of minima at points in the BZ different from the point $\boldsymbol{\Gamma}$.

model we find that $d_z(\boldsymbol{K}_A) = -M - 2\sqrt{3}t_2$ and $d_z(\boldsymbol{K}_B) = -M + 2\sqrt{3}t_2$. Thus, in the regime $t_2 > M/(2\sqrt{3})$, the phase acquired by the particle wrapping around the BZ does not vanish. In this case, according to the bulk-boundary correspondence [11], by fixing the chemical potential of the system to the gap between two bands, one should be able to observe edge modes that go across the boundary of our system in real space. These modes should disappear in the regime $t_2 < M/(2\sqrt{3})$, after moving through the topological phase transition at $t_2 = M/(2\sqrt{3})$, for which the gap between two bands closes and the system becomes conducting.

These calculations are verified numerically by diagonalizing the Hamiltonian in the strip geometry, i.e., with periodic boundaries along x and open boundaries along y (zigzag boundary conditions). The band structure is calculated for different values of t_2/M and edge modes are detected, as seen in Fig. 2. Moreover, we adapt methods previously used in works of Refs. [139,140] to derive an analytical calculation of the dispersion relation for edge modes of the anisotropic Haldane model, by considering an exponentially decaying ansatz. In Fig. 2(d), we compare the analytical and numerical solutions. We outline that if $t_2 > M/(2\sqrt{3})$, even weak values of t_2 (compared to t_1) and, as a consequence, small amplitudes of the Floquet perturbation V, permit one to observe edge modes.

IV. ENGINEERING A BOSONIC FFLO ANALOG

Topological properties of the (anisotropic) Haldane model described in the previous section can be probed in photonic systems [124–126] or with fermions at half-filling [35,41]. The system of bosons can, however, give access to the physics of unusual superfluids and Mott insulators [50,51,53]. Following Ref. [53], in this section we study properties of lattice bosons with artificial gauge fields in the anisotropic Haldane model. We show how the QPT between the uniform superfluid and the finite momentum BEC is affected by the anisotropy (by performing a comparison to the isotropic case studied in Ref. [53]) and we explore the effect of weak interactions in such a system.

Therefore, we consider the Hamiltonian $\hat{H} = \hat{H}_0 + \hat{H}_{\text{eff}}^{(1)} + \hat{H}_{\text{BH}}$, where

$$\hat{H}_0 = \epsilon_0\left(\sum_i \hat{a}_i^\dagger\hat{a}_i + \sum_j \hat{b}_j^\dagger\hat{b}_j\right) - t_1\sum_{\langle ij\rangle}(\hat{a}_i^\dagger\hat{b}_j + \hat{b}_j^\dagger\hat{a}_i),$$

$$\hat{H}_{\text{eff}}^{(1)} = -t_2\left(\sum_{\langle\langle ik\rangle\rangle}^{\text{anis}} e^{\pm\frac{i\pi}{2}}\hat{a}_i^\dagger\hat{a}_k + \sum_{\langle\langle jl\rangle\rangle}^{\text{anis}} e^{\pm\frac{i\pi}{2}}\hat{b}_j^\dagger\hat{b}_l + \text{H.c.}\right),$$

$$\hat{H}_{\text{BH}} = \frac{U}{2}\sum_i \hat{n}_i(\hat{n}_i - 1). \tag{14}$$

For the sake of clarity, we choose $\omega_A = \omega_B = \epsilon_0$, such that the Semenoff mass term $M = (\omega_A - \omega_B)/2$, producing charge density wave orders in real space, is zero. When interactions are absent or sufficiently weak, this system is characterized by the presence of two distinct phases corresponding to the formation of either a zero-momentum BEC (ZM phase) or a finite-momentum BEC (FM phase) analogous to FFLO states. These phases appear since the single-particle Hamiltonian has minima at different points in the lowest band, as depicted in Figs. 3 and 5. The ZM-FM transition between two phases is characterized by a change in the current patterns. We notice also that the nature of this transition is different in isotropic and anisotropic configurations of the Haldane model. In the first case the global minimum in the ZM phase transforms into a local maximum in the FM phase. Whereas in the second case the global minimum in the ZM phase still stays a minimum in the FM phase, but becomes local. This effect is due to the breaking of C_3 symmetry between two models. We outline also that considering a model with artificial gauge fields is the only possibility of observing the FM phase using s bands.

A. ZM phase

The ZM phase occurs as long as $t_2 < t_2^c = \sqrt{3/8}t_1$, while the isotropic model has a critical value $t_2^c = t_1/\sqrt{3}$. At zero temperature, bosons condense at zero momentum at the center $\mathbf{\Gamma}$ of the BZ, meaning that we can approximately write

$$\hat{a}_i \approx \frac{\hat{a}_{\mathbf{\Gamma}}}{\sqrt{N_c}}, \quad \hat{b}_j \approx \frac{\hat{b}_{\mathbf{\Gamma}}}{\sqrt{N_c}}. \tag{15}$$

Within this approximation, the Hamiltonian simplifies to

$$\begin{aligned}\hat{H} \approx\ & \epsilon_0(\hat{a}_{\mathbf{\Gamma}}^\dagger\hat{a}_{\mathbf{\Gamma}} + \hat{b}_{\mathbf{\Gamma}}^\dagger\hat{b}_{\mathbf{\Gamma}}) - 3t_1(\hat{a}_{\mathbf{\Gamma}}^\dagger\hat{b}_{\mathbf{\Gamma}} + \hat{b}_{\mathbf{\Gamma}}^\dagger\hat{a}_{\mathbf{\Gamma}}) \\ & + \frac{U}{2}\left[\hat{a}_{\mathbf{\Gamma}}^\dagger\hat{a}_{\mathbf{\Gamma}}\left(\frac{\hat{a}_{\mathbf{\Gamma}}^\dagger\hat{a}_{\mathbf{\Gamma}}}{N_c} - 1\right) + \hat{b}_{\mathbf{\Gamma}}^\dagger\hat{b}_{\mathbf{\Gamma}}\left(\frac{\hat{b}_{\mathbf{\Gamma}}^\dagger\hat{b}_{\mathbf{\Gamma}}}{N_c} - 1\right)\right].\end{aligned} \tag{16}$$

We next introduce the total number of sites $N_s = 2N_c$, the filling $n = N/N_s$ and the complex order parameter in sublattice A as $\langle\hat{a}_i\rangle = \langle\hat{a}_{\mathbf{\Gamma}}\rangle/\sqrt{N_c} = \sqrt{n}e^{i\theta_A}$, with a similar expression for sublattice B, assuming an equal filling in both sublattices. The superfluid phases $\theta_{A/B}$ in each sublattice are pinned by the t_1 hopping term, such that $\theta_A = \theta_B$. This corresponds to the presence of one Goldstone mode. The ground-state energy then reads

$$E_{\mathrm{GS}}^{\mathrm{ZM}} = N_s\left[(\epsilon_0 - 3t_1)n + \frac{U}{2}n(n-1)\right]. \tag{17}$$

We remark that the contribution of t_2 terms effectively vanishes in the ground state. The bond currents are defined as $J_{ii'} = -2\,\mathrm{Im}\,(t_{ii'}\,\langle\hat{a}_i^\dagger\hat{a}_{i'}\rangle)$ within sublattice A and similar expressions are used between sublattices A and B and within sublattice B. Here $t_{ii'}$ is the amplitude of the corresponding tunneling. In the ZM phase, currents between NNN sites in the direction of vectors $\boldsymbol{v}_1$ or $\boldsymbol{v}_2$ are proportional to t_2:

$$J_{AA,\boldsymbol{v}_1}^{\mathrm{ZM}} = J_{AA,\boldsymbol{v}_2}^{\mathrm{ZM}} = -2\,\mathrm{Im}\,(-it_2n) = 2nt_2. \tag{18}$$

In the anisotropic case we do not have NNN hoppings along $\boldsymbol{v}_3$, meaning that the corresponding currents are also always zero: $J_{AA,\boldsymbol{v}_3}^{\mathrm{ZM}} = 0$.

B. Excitations in the ZM phase (Bogoliubov transformation)

In this section we use the Bogoliubov transformation [141] to study excitations above the ground state in the ZM phase. When the temperature T is sufficiently low, one can suppose that the ground state at $\boldsymbol{k} = 0$ will be still macroscopically occupied by a population of $N_0 = n_0N_s$ bosons (with filling n_0). Small fluctuations can be described by operators $\hat{z}_{\nu,\boldsymbol{k}}$ with $\nu = a$ or b. The total number of particles is thus

$$N = N_0 + \sum_{\substack{\boldsymbol{k}\in\mathcal{BZ},\\ \boldsymbol{k}\neq 0,\nu}} \hat{z}_{\nu,\boldsymbol{k}}^\dagger\hat{z}_{\nu,\boldsymbol{k}}. \tag{19}$$

We are interested in writing the Hamiltonian $\hat{H}$ in powers of $\hat{z}_{\nu,\boldsymbol{k}}$. For convenience we also prefer to express $\hat{H}$ in the grand canonical ensemble, by introducing the chemical potential μ. To zero order in the perturbation we recognize the expression for the ground-state energy $E_{\mathrm{GS}}^{\mathrm{ZM}} - \mu N_0$.

The term linear in the fluctuation vanish for a particular value of the chemical potential, that is,

$$\mu = -3t_1 + Un_0. \tag{20}$$

To second order in perturbation we obtain

$$\begin{aligned}\hat{H}_2 =& \sum_{\substack{\boldsymbol{k}\in\mathcal{BZ},\\ \boldsymbol{k}\neq 0}} \begin{bmatrix}\hat{z}_{a,\boldsymbol{k}}^\dagger \\ \hat{z}_{b,\boldsymbol{k}}^\dagger\end{bmatrix}^t \cdot [-\boldsymbol{d}(\boldsymbol{k})\cdot\boldsymbol{\sigma} - \mu I_{2\times 2}] \cdot \begin{bmatrix}\hat{z}_{a,\boldsymbol{k}} \\ \hat{z}_{b,\boldsymbol{k}}\end{bmatrix} \\ & + \frac{Un_0}{2}\sum_{\substack{\boldsymbol{k}\in\mathcal{BZ},\\ \boldsymbol{k}\neq 0,\nu}} [\hat{z}_{\nu,\boldsymbol{k}}^\dagger\hat{z}_{\nu,-\boldsymbol{k}}^\dagger + \hat{z}_{\nu,\boldsymbol{k}}\hat{z}_{\nu,-\boldsymbol{k}} + 4\hat{z}_{\nu,\boldsymbol{k}}^\dagger\hat{z}_{\nu,\boldsymbol{k}}],\end{aligned} \tag{21}$$

where functions $d_j(\boldsymbol{k})$ are defined in Eq. (9). The resulting Hamiltonian can now be rewritten (up to some constant term E_0) as

$$\hat{H}_2 = -\frac{1}{2}\sum_{\boldsymbol{k}} \hat{Z}_{\boldsymbol{k}}^\dagger \cdot \mathcal{H}_{\mathrm{PH}}(\boldsymbol{k}) \cdot \hat{Z}_{\boldsymbol{k}}, \tag{22}$$

where $\hat{Z}_{\boldsymbol{k}}$ and $\mathcal{H}_{\mathrm{PH}}(\boldsymbol{k})$ are defined as follows:

$$\hat{Z}_{\boldsymbol{k}}^\dagger = [\hat{z}_{a,\boldsymbol{k}}^\dagger, \hat{z}_{b,\boldsymbol{k}}^\dagger, \hat{z}_{a,-\boldsymbol{k}}, \hat{z}_{b,-\boldsymbol{k}}], \tag{23}$$

$$\mathcal{H}_{\mathrm{PH}}(\boldsymbol{k}) = \begin{bmatrix} \mu + d_z(\boldsymbol{k}) - 2Un_0 & d_x(\boldsymbol{k}) - d_y(\boldsymbol{k})i & -Un_0 & 0 \\ d_x(\boldsymbol{k}) + d_y(\boldsymbol{k})i & \mu - d_z(\boldsymbol{k}) - 2Un_0 & 0 & -Un_0 \\ -Un_0 & 0 & \mu - d_z(\boldsymbol{k}) - 2Un_0 & d_x(\boldsymbol{k}) + d_y(\boldsymbol{k})i \\ 0 & -Un_0 & d_x(\boldsymbol{k}) - d_y(\boldsymbol{k})i & \mu + d_z(\boldsymbol{k}) - 2Un_0 \end{bmatrix}. \tag{24}$$

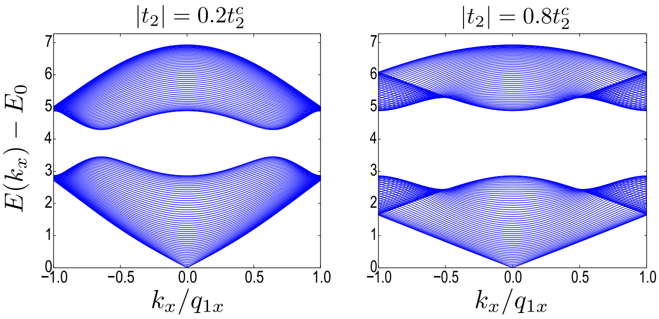

FIG. 4. Dispersion relation of excitations in the ZM phase of the anisotropic Haldane model, showing the linear Bogoliubov dispersion relation around the point $\mathbf{\Gamma}$ in the BZ. All figures were taken for $t_1 = 1$ and $n_0 U = 1$.

This Hamiltonian can be diagonalized by using the Bogoliubov transformation from the particle operators $\hat{z}_{\nu,\boldsymbol{k}}$ to quasiparticle operators $\hat{\xi}_{\nu,\boldsymbol{k}}$. Transformed operators should preserve the bosonic commutation relations:

$$\left[\hat{\xi}^{\dagger}_{\nu_1,\boldsymbol{k}_1},\hat{\xi}_{\nu_2,\boldsymbol{k}_2}\right] = \delta_{\boldsymbol{k}_1\boldsymbol{k}_2}\delta_{\nu_1\nu_2}, \tag{25}$$

$$\left[\hat{\xi}_{\nu_1,\boldsymbol{k}_1},\hat{\xi}_{\nu_2,\boldsymbol{k}_2}\right] = 0. \tag{26}$$

In the matrix notation this transformation can be written as $\hat{Z}_{\boldsymbol{k}} = T_{\boldsymbol{k}} \cdot \hat{\Xi}_{\boldsymbol{k}}$. The condition of preserving commutation relations imposes restrictions on the form of $T_{\boldsymbol{k}}$. It should verify

$$T_{\boldsymbol{k}} \cdot \Sigma \cdot T_{\boldsymbol{k}}^{\dagger} = T_{\boldsymbol{k}}^{\dagger} \cdot \Sigma \cdot T_{\boldsymbol{k}} = \Sigma = \begin{bmatrix} I_2 & 0 \\ 0 & -I_2 \end{bmatrix}. \tag{27}$$

Our goal consists then in finding a transformation $T_{\boldsymbol{k}}$ that could diagonalize the Hamiltonian: $T_{\boldsymbol{k}}^{\dagger} \cdot \mathcal{H}_{\mathrm{PH}}(\boldsymbol{k}) \cdot T_{\boldsymbol{k}} = \mathcal{D}(\boldsymbol{k})$. If such a transformation exists in spite of constraints imposed by Eq. (27), eigenvalues of the matrix $\Sigma\mathcal{D}(\boldsymbol{k})$ will correspond to the spectrum of Bogoliubov pseudoparticles. One can then use the following identity: $T_{\boldsymbol{k}}^{-1}\Sigma\mathcal{H}_{\mathrm{PH}}(\boldsymbol{k})T_{\boldsymbol{k}} = \Sigma\mathcal{D}(\boldsymbol{k})$ to deduce that matrices $\Sigma\mathcal{H}_{\mathrm{PH}}(\boldsymbol{k})$ and $\Sigma\mathcal{D}(\boldsymbol{k})$ are similar. Thus, in order to obtain the Bogoliubov spectrum we only need to diagonalize $\Sigma\mathcal{H}_{\mathrm{PH}}(\boldsymbol{k})$.

In Fig. 4 we show the corresponding solution for the anisotropic Haldane-like model at the value of the interaction such that $n_0 U = t_1 = 1$. The dispersion relation is linear around the point $\boldsymbol{k} = 0$. We remark that in the anisotropic case the velocity of the "sound" mode depends on t_2, whereas in the isotropic case it was completely independent of t_2. In Ref. [142] it was shown for the case of the isotropic Haldane model, that topological properties of Bloch bands present in the noninteracting case are smoothly carried over to Bogoliubov excitation bands in the ZM phase. We expect the same formalism to be applicable to the case of the anisotropic Haldane model and in the FM phase.

C. Critical value of the NNN hopping amplitude

As we increase the ratio t_2/t_1 up to some critical value, the minimum of the single-particle band structure at the point $\mathbf{\Gamma}$ splits into two new minima that then start moving away from the center of the BZ. Numerical simulations of the Fig. 3 and symmetry arguments imply that for any value of t_2/t_1, the position of minima along the y axis does not change. Thus, it should be sufficient for us to perform calculations only along the $k_y = 0$ axis in the BZ. In Fig. 5 we show some examples of the analytical energy structure compared to results of ED simulations for the one-particle Hamiltonian in different regimes of t_2 for $k_y = 0$, $k_x \in [0,4\pi/\sqrt{3}a]$.

The goal of this subsection is to deduce the precise value of the critical NNN hopping amplitude t_2^c. Let us consider that the condensation in the general case occurs at points $\boldsymbol{k} = \pm(z\pi/\sqrt{3}a)\boldsymbol{e}_x$, for some real $z \in [0,2]$, defined up to a reciprocal lattice vector. Eigenvalues of the one-particle Hamiltonian $\hat{H}_{1p}$ at these points are

$$\epsilon_{\pm}(z) = \epsilon_0 \pm \sqrt{5t_1^2 + \left(16t_2^2 - 4t_1^2\right)\sin^2\left(\frac{\pi z}{2}\right) + 4t_1^2\cos\left(\frac{\pi z}{2}\right)}. \tag{28}$$

Extrema of the lower band energy correspond to zeros of $\frac{\partial\epsilon_-(z)}{\partial z}$, which we will denote by z_c. They are solutions of the following set of equations:

$$\sin\left(\frac{\pi z_c}{2}\right) = 0,$$
$$\cos\left(\frac{\pi z_c}{2}\right) = \frac{1}{2}\left(\frac{t_1^2}{4t_2^2 - t_1^2}\right). \tag{29}$$

We deduce three main regimes in the evolution of the energy band structure along the $k_y = 0$ line.

The first regime is determined by $|t_2| < \sqrt{1/8}t_1$. In this region the solution of the second equation exists and corresponds to the maximum of the band at two Dirac points. If we increase t_2, starting from zero, the value of z_c corresponding to these maxima increases (Dirac points move away from extremities of the BZ) until it reaches the value $z_c = 2$. The minimum of the band is localized at the point $\mathbf{\Gamma}$, which corresponds to the solution of the first equation for $z_c = 0$.

In the region $\sqrt{1/8}t_1 < |t_2| < \sqrt{3/8}t_1$ there is no solution of the second equation and the band possesses only one minimum at $z_c = 0$ and maximum at $z_c = 2$.

In the region $|t_2| > \sqrt{3/8}t_1$ the solution of the second equation starts existing again and corresponds to two new minima of the band. At the same time, the solution of the first equation at $z_c = 0$ transforms into a local maximum and the solution at $z_c = 2$ stays a global maximum of the band. This defines the precise point of the ZM-FM transition: $t_2^c = \sqrt{3/8}t_1$.

The transition between all these three regimes can be clearly seen in Fig. 5 (upper panel). The shape of the energy band at the critical point, expressed in terms of the parameter z is

$$\epsilon_-(z) \underset{z\to 0}{\approx} \epsilon_0 - 3t_1 + \frac{t_1}{12}\left(\frac{\pi z}{2}\right)^4. \tag{30}$$

Thus, at the transition the well becomes much wider: The second power in the dispersion relation is replaced by the fourth power. In the following we will study more closely the behavior of the time-dependent system in the regime of the effective NNN hopping amplitude t_2 close to t_2^c. However, in order to

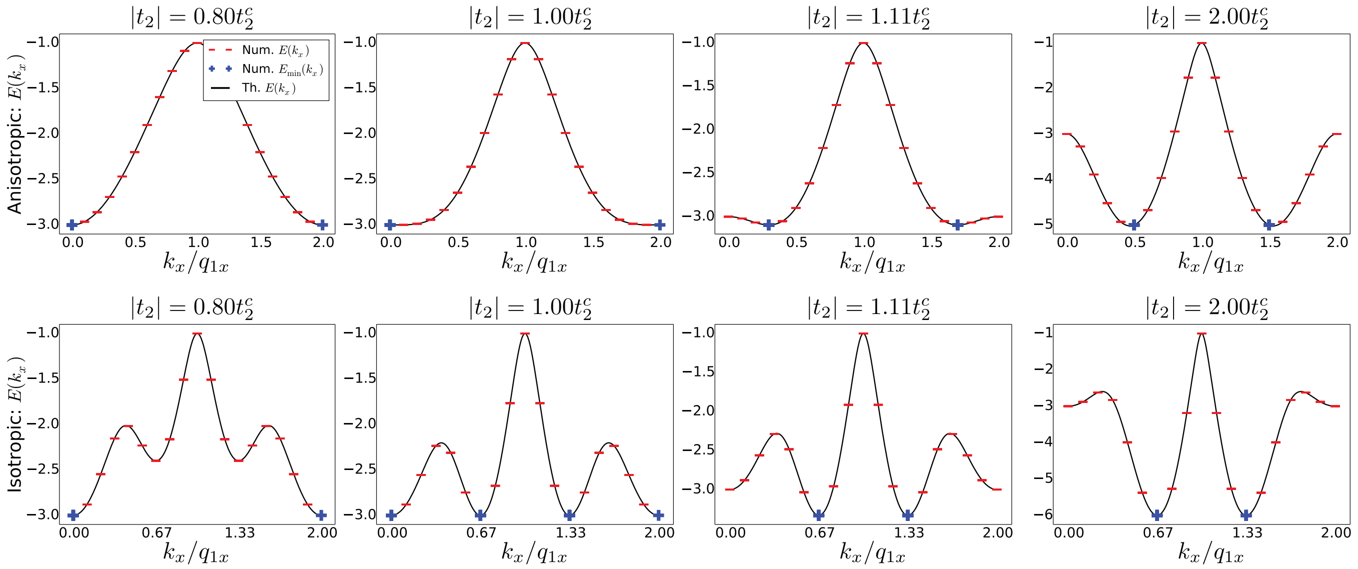

FIG. 5. Cut of the lowest energy band of the single-particle system along the $k_y = 0$ line. Analytical calculations (black solid line) are superposed to the results of ED (red dashes). (Upper panel) Anisotropic model. Structure of the ED cluster is 10×2 cells (40 sites) with tilt $t_h = -1$. Values of t_2 are chosen is such a way that the condensation occurs precisely at the points allowed by the geometry of the ED cluster. The value $t_2 = 2t_2^c$ is high enough to see the physics of the $t_2 \gg t_2^c$ regime. In this last case, shown in the rightmost figure, only the small distinction between analytical and numerical results (due to finite size effects) is observed. (Lower panel) Isotropic model. Structure of the ED cluster is 9×2 cells (36 sites) with tilt $t_h = -1$.

give an estimation for required experimental parameters, we calculate the critical value V_c needed to reach the ZM-FM phase transition at a fixed frequency: $V_c(\omega = 60t_1) \approx 8.57t_1$.

Displacement of the condensation point for different parameters of the problem affects the procedure of the numerical ED. Numerical simulations of the infinite lattice requires considering a particular set of points on the lattice, forming a cluster, and of periodic boundary conditions gluing together different clusters. This defines the set of quantum numbers associated with irreducible representations of the group of translations along two Bravais vectors of the lattice. Each quantum number corresponds to one point in the BZ and the amount of quantum numbers equals the number of possible translations in the cluster. Thus, by increasing the cluster size, we increase the resolution in the BZ.

According to our previous discussion, in order to capture the ZM-FM transition in the anisotropic model, one can restrict ourselves to the case $k_y = 0$. This motivates us to consider a particular choice of clusters, maximizing the resolution in the BZ along k_x with the price of minimizing the resolution along k_y. We make such clusters by composing $l_x \times l_y$ unit cells of the honeycomb lattice in the geometry of the parallelogram generated by vectors $l_x \boldsymbol{v}_3$ and $l_y \boldsymbol{v}_1$. Each parallelogram is then translated with spanning vectors $\boldsymbol{s}_1 = l_x \boldsymbol{v}_3$ and $\boldsymbol{s}_2 = l_y \boldsymbol{v}_1 - t_h \boldsymbol{v}_3$ to fill the full lattice. Here t_h denotes the tilt. This defines our implementation of PBC. Example of such tilted cluster is shown in Fig. 6.

D. FM phase

The FM phase arises when t_2 reaches the critical value $t_2^c = \sqrt{3/8}t_1$. In the limit $t_2 \gg t_1$, the two sublattices become decoupled and bosons condense at the two inequivalent points $\boldsymbol{K}_A = (\pi/\sqrt{3}a)\boldsymbol{e}_x$ (on sublattice A), and $\boldsymbol{K}_B = -(\pi/\sqrt{3}a)\boldsymbol{e}_x$ (on sublattice B), as shown on Fig. 3(c). We begin with the study of the properties of the finite momentum BEC, by considering first this simpler case.

1. *FM phase in the regime of decoupled sublattices*

In the limit of two decoupled sublattices, one can use the following approximation for the real space annihilation (and creation) operators:

$$\hat{a}_i \approx \frac{e^{-i\boldsymbol{r}_i \boldsymbol{K}_A}}{\sqrt{N_c}} \hat{a}_{\boldsymbol{K}_A}, \quad \hat{b}_j \approx \frac{e^{-i\boldsymbol{r}_j \boldsymbol{K}_B}}{\sqrt{N_c}} \hat{b}_{\boldsymbol{K}_B}. \tag{31}$$

In the following we will also use the notation,

$$\langle \hat{a}_i^\dagger \hat{a}_i \rangle = n_A = N_A/N_c, \quad \langle \hat{b}_j^\dagger \hat{b}_j \rangle = n_B = N_B/N_c, \tag{32}$$

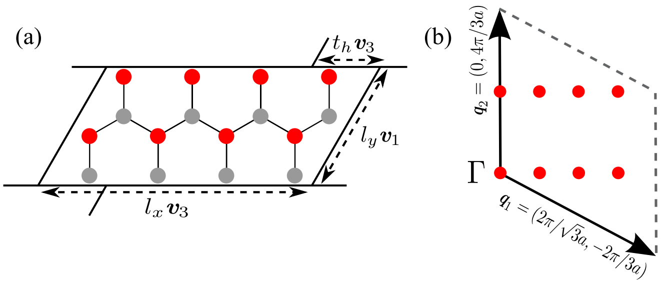

FIG. 6. (a) Schematic representation of the tilted cluster with 4×2 cells and with the tilt $t_h = -1$, used in ED simulations of the ZM-FM phase transition. Black lines determine boundary of each cluster. (b) Corresponding quantum numbers allowed by symmetries of the cluster.

such that $(n_A + n_B)/2 = n = N/N_s$ is the filling, since $N_c = N_s/2$. Within the mean-field approximation, we simply write

$$\langle \hat{a}_{\boldsymbol{K}_A} \rangle \approx \sqrt{N_A} e^{i\theta_A}, \quad \langle \hat{b}_{\boldsymbol{K}_B} \rangle \approx \sqrt{N_B} e^{i\theta_B}, \tag{33}$$

where θ_A and θ_B are the superfluid phases associated with the two condensates. One can easily check that in the ground state the contribution of the NN hopping term vanishes in the thermodynamic limit:

$$\begin{aligned} \sum_{\langle ij \rangle} \hat{a}_i^\dagger \hat{b}_j &\propto \sum_i \left(e^{-i\boldsymbol{K}_B \mathbf{r}_i} \sum_{j=1}^{3} e^{-i\boldsymbol{K}_B \mathbf{u}_j} \hat{a}_i^\dagger \hat{b}_{\boldsymbol{K}_B} \right) \\ &= \sum_i e^{i(\boldsymbol{K}_A - \boldsymbol{K}_B)\mathbf{r}_i} \hat{a}^\dagger_{\boldsymbol{K}_A} \hat{b}_{\boldsymbol{K}_B} = 0. \end{aligned} \tag{34}$$

We thus see that the contribution of the t_1 term effectively vanishes in the ground state. Finally, we obtain that in the regime $t_2 \gg t_2^c$, the mean-field approximation simplifies the Hamiltonian into

$$\begin{aligned} \hat{H} \approx& (\epsilon_0 - 4t_2 - U/2)\big(\hat{a}^\dagger_{\boldsymbol{K}_A} \hat{a}_{\boldsymbol{K}_A} + \hat{b}^\dagger_{\boldsymbol{K}_B} \hat{b}_{\boldsymbol{K}_B}\big) \\ &+ \frac{U}{N_s}\big[\big(\hat{a}^\dagger_{\boldsymbol{K}_A} \hat{a}_{\boldsymbol{K}_A}\big)^2 + \big(\hat{b}^\dagger_{\boldsymbol{K}_B} \hat{b}_{\boldsymbol{K}_B}\big)^2\big], \end{aligned} \tag{35}$$

so that the ground-state energy reads

$$E_{\mathrm{GS}}^{\mathrm{FM}} \underset{t_2 \gg t_2^c}{=} N_s\big[(\epsilon_0 - 4t_2 - U/2)n + U\big(n_A^2 + n_B^2\big)/4\big]. \tag{36}$$

As the two sublattices are completely decoupled, both phases θ_A and θ_B become independent parameters, which corresponds to the presence of two Goldstone modes.

The phase difference $\theta_A - \theta_B$ can be fixed if a coherent coupling between the two wells is generated, resulting in a modification of J_{AA} and allowing for finite intersublattice currents J_{AB}. Such effect can be induced, for example, by adding impurities to the model or, in the thermodynamic limit, by taking into account quantum fluctuations via the so-called "order by disorder" mechanism [143]. This problem was studied in detail in Ref. [53] in the case of the isotropic Haldane model, and it will not be considered in this work. In numerical simulations, we also do not observe this effect since the ground state obtained using ED corresponds to the state without coherent coupling. In particular, NN currents J_{AB} calculated in the ground state using ED will always be zero. As a consequence, in the following we will refer to the relatively simple case of two condensates at $\boldsymbol{K}_A$ and $\boldsymbol{K}_B$, which are completely decoupled. This leads in particular to the conclusion that in the $t_2 \gg t_2^c$ regime of the FM phase NNN currents are simply zero:

$$J^{\mathrm{FM}}_{AA,\boldsymbol{v}_j} \underset{t_2 \gg t_2^c}{=} 0. \tag{37}$$

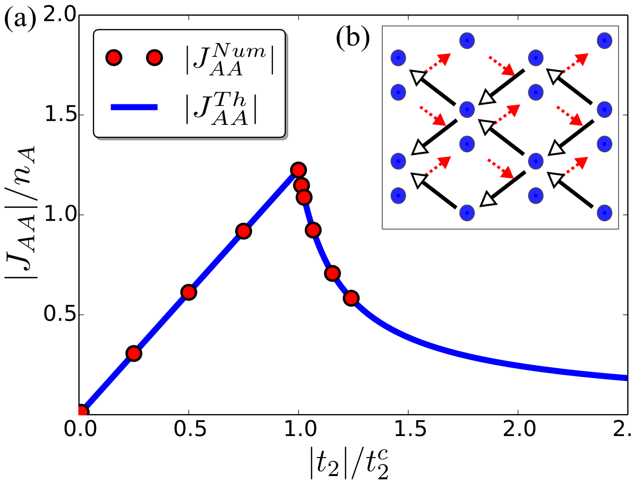

FIG. 7. (a) Variation of the second neighbor current J_{AA} with t_2. Qualitative change of behavior can be seen when crossing the critical value $t_2^c = \sqrt{3/8}t_1$. In the figure analytical prediction (blue line) is compared with the results of ED (red circles). (b) Result of ED showing patterns of currents J_{AA}. Closed loops of chiral currents involve lozenge geometries. Different types of arrows correspond to different sublattices.

2. FM phase in the intermediate regime

We now consider the more realistic case when t_2 becomes of the order of t_1 in the $t_2 > t_2^c$ regime. We then define $\hat{\alpha}_{\boldsymbol{k}}$ and $\hat{\beta}_{\boldsymbol{k}}$ the annihilation operators in the lower and upper energy bands of the single-particle Hamiltonian. At each point of the BZ these operators are related to $\hat{a}_{\boldsymbol{k}}$ and $\hat{b}_{\boldsymbol{k}}$ through some unitary transformation:

$$\begin{aligned} \hat{a}_{\boldsymbol{k}} &= \mu(\boldsymbol{k})\hat{\alpha}_{\boldsymbol{k}} + \nu(\boldsymbol{k})\hat{\beta}_{\boldsymbol{k}}, \\ \hat{b}_{\boldsymbol{k}} &= e^{i\phi(\boldsymbol{k})}[-\nu^*(\boldsymbol{k})\hat{\alpha}_{\boldsymbol{k}} + \mu^*(\boldsymbol{k})\hat{\beta}_{\boldsymbol{k}}], \end{aligned} \tag{38}$$

with $|\mu(\boldsymbol{k})|^2 + |\nu(\boldsymbol{k})|^2 = 1$. In the low temperature limit, bosons condense at points $\pm\boldsymbol{K}_c = \pm(z_c\pi/\sqrt{3}a)\boldsymbol{e}_x$ (we recall that by our definition $z_c > 0$) so that $\langle \hat{\alpha}_{\pm\boldsymbol{K}_c} \rangle \sim \sqrt{N}$ and $\langle \hat{\beta}_{\pm\boldsymbol{K}_c} \rangle = 0$. Thus, annihilation (and creation) operators in the real space are approximated by

$$\begin{aligned} \hat{a}_i &\approx \frac{e^{-i\boldsymbol{K}_c\boldsymbol{r}_i}\hat{a}_{\boldsymbol{K}_c} + e^{i\boldsymbol{K}_c\boldsymbol{r}_i}\hat{a}_{-\boldsymbol{K}_c}}{\sqrt{N_c}}, \\ \hat{b}_i &\approx \frac{e^{-i\boldsymbol{K}_c\boldsymbol{r}_i}\hat{b}_{\boldsymbol{K}_c} + e^{i\boldsymbol{K}_c\boldsymbol{r}_i}\hat{b}_{-\boldsymbol{K}_c}}{\sqrt{N_c}}. \end{aligned} \tag{39}$$

We then introduce the averages,

$$\langle \hat{a}_{\pm\boldsymbol{K}_c} \rangle = \sqrt{N_{A,\pm}} e^{i\theta_{A,\pm}}, \quad \langle \hat{b}_{\pm\boldsymbol{K}_c} \rangle = \sqrt{N_{B,\pm}} e^{i\theta_{B,\pm}}, \tag{40}$$

such that $N_{A,+} + N_{A,-} = N_A$, $N_{B,+} + N_{B,-} = N_B$, $N_{A,\pm} + N_{B,\pm} = N_\pm$, and $N_A + N_B = N_+ + N_- = N$. The approximation (39) can be used to find a more general form of the GS Hamiltonian and GS energy in the FM phase (see Appendix B for their complete expressions). Moreover, we obtain that phases $\theta_{A,\pm}$ and $\theta_{B,\pm}$ are pinned pair by pairs, which corresponds to the presence of two Goldstone modes. We also get the expression of currents valid in both regimes of t_2.

$$\begin{aligned} J_{AA,\boldsymbol{v}_1} &= J_{AA,\boldsymbol{v}_2} = -t_2\frac{N_A}{N_c}\cos\left(z_c\frac{\pi}{2}\right), \\ J_{AA,\boldsymbol{v}_3} &= 0. \end{aligned} \tag{41}$$

The evolution of the currents J_{AA} with t_2 is shown in Fig. 7, where the analytical prediction is compared with the results of ED in a weakly interacting regime.

Another way to perform a numerical verification of the behavior of the system in the FM regime is to look at

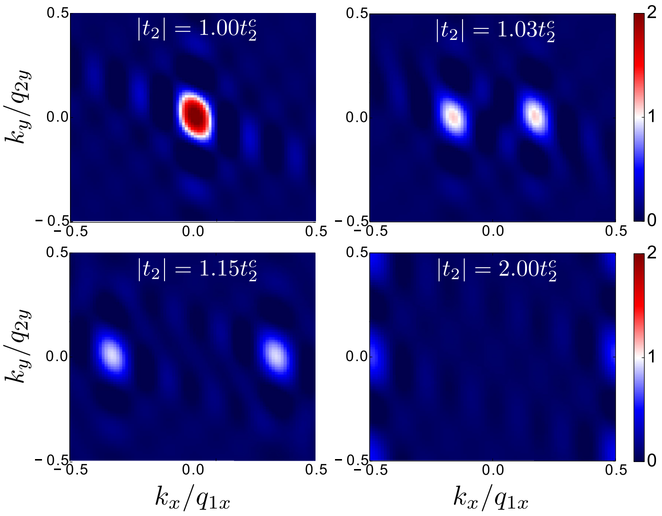

FIG. 8. Momentum distribution $n(\boldsymbol{k})$ at the transition in the FM phase in the bosonic many-body ground state. Structure of the ED cluster is 6×4 cells (48 sites) with tilt $t_h = -2$. Parameters of simulations are as follows: $N = 2$, $U = 0$. Finite size effects result in a tilt of the maxima of $n(\boldsymbol{k})$ and its nonphysical oscillations.

the momentum distribution $n(\boldsymbol{k})$. In Fig. 8, we give some results of ED showing how the momentum distribution in the many-body GS in the $\mathbf{k} = 0$ sector evolves when changing t_2 above the critical value t_2^c. We effectively observe the splitting of the condensation point into two points and their further displacement along the $k_y = 0$ line.

The continuous variation of currents suggests that the ZM-FM transition in the anisotropic Haldane model is of the second order. In order to justify this point, we first write explicitly the unitary transformation of Eq. (38) at momentum $\pm\boldsymbol{K}_c$ in terms of z_c:

$$\hat{a}_{\pm\boldsymbol{K}_c} = -\sqrt{\frac{\sqrt{X^2(z_c)+Y^2(z_c)} \pm Y(z_c)}{2\sqrt{X^2(z_c)+Y^2(z_c)}}}\,\hat{\alpha}_{\pm\boldsymbol{K}_c} + \sqrt{\frac{\sqrt{X^2(z_c)+Y^2(z_c)} \mp Y(z_c)}{2\sqrt{X^2(z_c)+Y^2(z_c)}}}\,\hat{\beta}_{\pm\boldsymbol{K}_c},$$

$$\hat{b}_{\pm\boldsymbol{K}_c} = -\sqrt{\frac{\sqrt{X^2(z_c)+Y^2(z_c)} \mp Y(z_c)}{2\sqrt{X^2(z_c)+Y^2(z_c)}}}\,\hat{\alpha}_{\pm\boldsymbol{K}_c} - \sqrt{\frac{\sqrt{X^2(z_c)+Y^2(z_c)} \pm Y(z_c)}{2\sqrt{X^2(z_c)+Y^2(z_c)}}}\,\hat{\beta}_{\pm\boldsymbol{K}_c}, \tag{42}$$

where $X(z_c)$ and $Y(z_c)$ are defined as follows:

$$X(z_c) = t_1\left[1 + 2\cos\left(z_c\frac{\pi}{2}\right)\right],$$

$$Y(z_c) = 4t_2 \sin\left(z_c\frac{\pi}{2}\right). \tag{43}$$

One notices that N_+ and N_-, corresponding to the number of particles in the wells at $\pm\boldsymbol{K}_c$, and z_c are the only parameters of the problem. In Eq. (B6), we express the GS energy in terms of these quantities. Close to the ZM-FM phase transition, we expand the GS energy in powers of z_c. By doing this calculation in the noninteracting case we obtain

$$E_{\mathrm{GS}} \underset{z_c \to 0}{=} \mathrm{cst} - t_1 N\left[\frac{8}{3}\left(\frac{t_2}{t_1}\right)^2 - 1\right]\left(\frac{\pi z_c}{2}\right)^2 + \frac{N}{108t_1^3}\left(128t_2^4 - 9t_1^4\right)\left(\frac{\pi z_c}{2}\right)^4 + \cdots. \tag{44}$$

The sign change of the first term, proportional to z_c^2, occurs at the value $t_2^c = \sqrt{3/8}t_1$, in agreement with our previous estimations. Moreover, the sign of the second term, proportional to z_c^4, is always positive in the FM phase. Thus, we clearly see that the transition in the anisotropic Haldane model is of the second order. This is different from the case of the isotropic Haldane model [53,144], where the transition is of the first order, since three wells are simultaneously present at the transition.

E. Effect of interactions on the QPT

In order to study more precisely the effect of interactions on the ZM-FM phase transition, we repeat the previous analysis and write down the contribution to the GS energy in powers of z_c associated with the interaction term only. This calculation is based on the ansatz (39). Thus, we must assume that interactions are weak enough so that they do not affect the two-well structure of the system in the FM phase. The result of such a calculation is given in Eq. (B6) of Appendix B.

First, we see that in the FM phase interactions imposes constraints onto N_+ and N_-—the numbers of particles in each well, and removes the degeneracy that was present in the noninteracting system. However, contrary to the most intuitive guess, there are two ground states that minimize the energy in two distinct subregimes of the FM phase: for $t_2^c < t_2 < \sqrt{(17+\sqrt{97})/24}\ t_2^c$ interactions favor particles in one particular well, such that either N_+ or N_- becomes precisely equal to N. When $t_2 > \sqrt{(17+\sqrt{97})/24}\ t_2^c$ the uniform distribution of particles $N_+ = N_- = N/2$ is preferred.

The second effect of weak interactions consists of moving the position of minima away from $\pm\boldsymbol{K}_c$. In particular, to the lowest order in z_c, the contribution of interactions to the GS energy at the SF-CSF transition is

$$\Delta E'_{\mathrm{GS}} = NUn\frac{8t_2^2}{9t_1^2}\left(z_c\frac{\pi}{2}\right)^2. \tag{45}$$

This leads to the increase of the critical NNN coupling amplitude t_2^c. If particles are not located all in one well, there appears an additional contribution,

$$\Delta E''_{\mathrm{GS}} = -\frac{16U}{3}\frac{N_+(N-N_+)}{N_s}\left(\frac{t_2}{t_1}\right)^2\left(z_c\frac{\pi}{2}\right)^2, \tag{46}$$

that, on the opposite, tends to decrease t_2^c. The second contribution $\Delta E''_{GS}$ dominates when $N_+ = N_- = N/2$, resulting in the generation of an effective repulsion between the two wells (see also Appendix B for a more detailed analysis).

In order to check our theoretical predictions, we perform ED calculations. We plot the many-body energy levels $E_i(k_x) - E_0$ for different values of the total momentum $\boldsymbol{k}$ (here

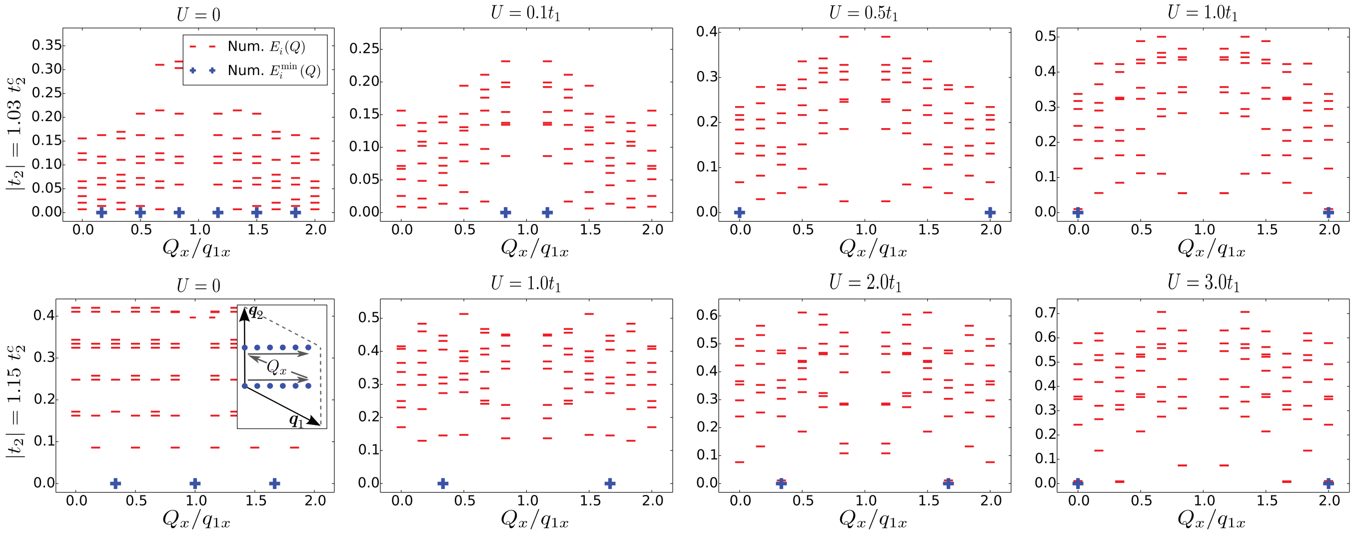

FIG. 9. Many-body energy levels (cut along the $k_y = 0$ line in the BZ). ED cluster is 6×2 cells (24 sites). Position in the BZ of quantum number associated with this precise cluster is shown on a small replica of Fig. 6(b). Different columns correspond to different values of U. Different lines correspond to different values of t_2. Parameters are $N = 5$ particles.

E_0 denotes the lowest energy over all momentum sectors). Simulation results are shown in Fig. 9 for an odd number of particles and Fig. 10 for an even number of particles.

Without interactions, we observe a high degeneracy of the many-body ground state due to the fact that all bosons condense independently in one of the two wells. If one increases the interaction strength, this degeneracy is lifted. We observe that, close to the transition ($t_2 \approx t_2^c$) in the FM phase, the most energetically favored ground state of the weakly interacting regime corresponds to the state with all particles condensed in the same well. This is not the case for higher values of t_2. If t_2 increases, the ground state becomes, as expected, the state with all particles uniformly distributed over two wells (with $N_+ - N_- = \pm 1$ if N is odd). The value at which this transition occurs agrees well with the analytical prediction $t_2 = \sqrt{(17 + \sqrt{97})/24}\ t_2^c$, with some imprecision coming from finite size effects.

When U increases, the ground state changes into a more complicated many-body state with $n(\boldsymbol{k})$ having a nonzero contribution at the $\boldsymbol{\Gamma}$ point. This transition is accompanied by the change of the location of the minimum in momentum space. In this regime the perturbation due to interactions cannot be interpreted as small in terms of other parameters of our problem. The effect of interactions in this nonperturbative regime will not be considered in this work.

In simulations we do not observe the displacement of the condensation point due to interactions. This is explained by the fact that for weak interactions this effect is not noticeable

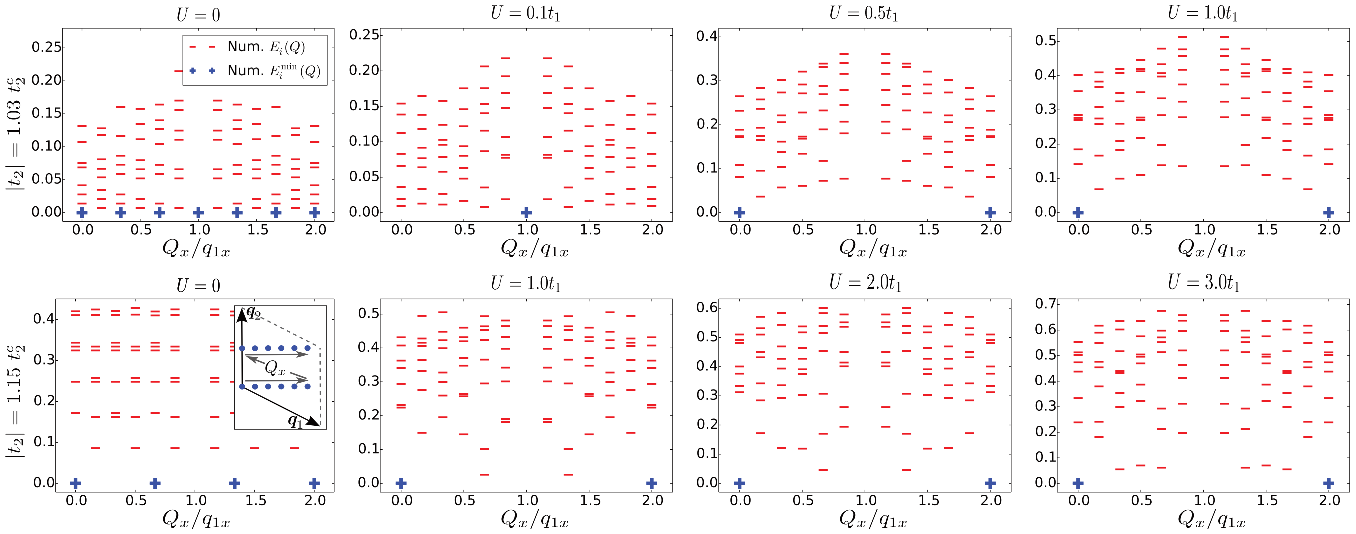

FIG. 10. Many-body energy levels (cut along the $k_y = 0$ line in the BZ). Energy minima are shown in blue. ED cluster is 6×2 cells (24 sites); the tilt $t_h = -1$. Position in the BZ of quantum number associated with this precise cluster is shown on a small replica of Fig. 6(b). Different columns correspond to different values of U. Different lines correspond to different values of t_2. Parameters are $N = 6$ particles.

enough to be observed because of the finite sizes of ED clusters, whereas in the regime of stronger interactions other effects occur earlier.

V. VALIDITY OF THE HFE CONVERGENCE

We recall that all properties of the anisotropic Haldane model studied in Secs. III B and IV correspond to the effective Hamiltonian (3), which we expand only up to the first order with contribution $\hat{H}_{\mathrm{eff}}^{(1)}$. In this section, we determine the conditions of validity for this approximation. More precisely, we want to compare the evolution of the system with the exact time-dependent Hamiltonian $\hat{H}(t)$ of Eq. (1) to the evolution with the effective Hamiltonian of the anisotropic Haldane model.

A. Second-order terms in the HFE

In order to study in detail the convergence of the HFE, one needs to evaluate higher order terms in this perturbative expansion (3). In our case, i.e., for the time-dependent perturbation $\hat{V}(t)$ with only two nonvanishing Fourier components $\hat{V}^{(\pm 1)}$, the second-order term is determined using the following identity [71–75]:

$$\hat{H}_{\mathrm{eff}}^{(2)} = \frac{1}{2\omega^2}([[\hat{V}^{(1)},\hat{H}_0],\hat{V}^{(-1)}] + \mathrm{H.c.}). \tag{47}$$

We study separately contributions coming from the term of frequencies (chemical potentials) ω_A and ω_B and the term of NN hoppings t_1, that are present in $\hat{H}_0$, and we denote them, respectively, by $\hat{H}_{\mathrm{eff}}^{(2)}(\omega_B - \omega_A)$ and $\hat{H}_{\mathrm{eff}}^{(2)}(t_1)$.

If we consider the choice of phases depicted in Fig. 1, the only effect of $\hat{H}_{\mathrm{eff}}^{(2)}(\omega_B - \omega_A)$ consists of an asymmetric renormalization of chemical potentials, resulting in the generation of an effective Semenoff mass term [138]. This effect vanishes if $\omega \gg \omega_A - \omega_B$. $\hat{H}_{\mathrm{eff}}^{(2)}(t_1)$ generates NN and NNNN hoppings with complex amplitudes, which can be used in particular to obtain Chern insulators with Chern number greater than 1. It also becomes irrelevant when $\omega \gg t_1$.

Moreover, if we consider the case of the many-body system with interactions weak enough, such that the Floquet approximation and the HFE are still valid, the interaction-dependent term $\hat{H}_{\mathrm{eff}}^{(2)}(U)$ will also appear at the second order in the perturbation theory. This term will lead to the generation of density-mediated NNN hoppings and second-order hoppings such that two particles move to or from one particular lattice site at the same time. This term becomes negligible when $\omega \gg U$.

$$\begin{aligned}
\hat{H}_{\mathrm{eff}}^{(2)}(\omega_B - \omega_A) &= \frac{V^2}{2\omega}\left(\frac{\omega_B - \omega_A}{\omega}\right)\left[\sum_{\langle\langle ik\rangle\rangle}\cos(\Theta_{ik})(\hat{a}_i^\dagger\hat{a}_k + \hat{a}_k^\dagger\hat{a}_i) - \sum_{\langle\langle jl\rangle\rangle}\cos(\Theta_{jl})(\hat{b}_j^\dagger\hat{b}_l + \hat{b}_l^\dagger\hat{b}_j)\right],\\
\hat{H}_{\mathrm{eff}}^{(2)}(t_1) &= \frac{V^2}{2\omega}\left(\frac{t_1}{\omega}\right)(\text{NN and NNNN hoppings with complex amplitudes}),\\
\hat{H}_{\mathrm{eff}}^{(2)}(U) &= \frac{V^2}{2\omega}\left(\frac{U}{\omega}\right)(\text{density-mediated NNN hoppings and second-order hoppings with complex amplitudes}).
\end{aligned} \tag{48}$$

B. Numerical convergence

We estimate more quantitatively, which values of the modulation frequency ω are big enough, compared to t_1 and U, so that we can neglect all second-contributions in the HFE. For clarity, we consider the case of $\omega_A = \omega_B$, such that the term $\hat{H}_{\mathrm{eff}}^{(2)}(\omega_B - \omega_A)$ is exactly zero. Therefore, we perform numerical simulations of the exact time evolution of the model. We initially prepare the system in the state $|\Psi(t=0)\rangle = |\Psi_0\rangle$ (in the following we will consider three different choices for this initial state) and we use the exact diagonalization technique to calculate states $|\Psi(t)\rangle$ and $|\Psi_{\mathrm{eff}}(t)\rangle$ at time t, evolved with $\hat{H}(t)$ and $\hat{H}_{\mathrm{eff}}$, respectively, where the last Hamiltonian is calculated up to the first order in the HFE (and thus corresponds to the Hamiltonian of the anisotropic Haldane model). As far as two states propagate in time, they deviate one from another. This deviation is captured by the "fidelity" $F(t)$ defined as follows:

$$F(t) = |\langle\Psi(t)\,|\,\Psi_{\mathrm{eff}}(t)\rangle|. \tag{49}$$

From the results of Sec. IV, we notice that we are also interested in the regime where the effectively generated NNN hopping amplitude $t_2 = \frac{V^2}{2\omega}$ becomes of the order of t_1, which implies that it means that the amplitude V behaves as $\sqrt{\omega t_1}$ in the limit $\omega \to \infty$. Thus, in order to have a more complete description, we perform simulations for different values of t_2. Once t_2 is fixed, we deduce the value of the Floquet modulation amplitude using relation $V = \sqrt{2\omega t_2}$. In particular, the critical value V_c required to reach the ZM-FM transition (according to the results of Sec. IV D) at fixed frequency $\omega = 60t_1$ is $V_c \approx 8.57t_1$.

To start with, we show the calculations performed in the single-particle case. Figure 11 represents the typical shape of the fidelity for the time evolution over 100 periods. The first important observation is related to the fast oscillation of $F(t)$, forming an "envelop" for its propagation in time. These oscillations are due to intraperiodic submotions of the system, not captured by $\hat{H}_{\mathrm{eff}}$, but described by Kick operators $\hat{K}_{\mathrm{eff}}$ (in agreement and according to the definition of Refs. [71–75]).

Secondly, during the time evolution over an integer number of periods, the value of intraperiodic maxima of $F(t)$ decreases. This effect originates from higher order terms in the HFE. Errors due to neglected terms are accumulated during each period, leading to an exponential decrease of $F(t)$ with

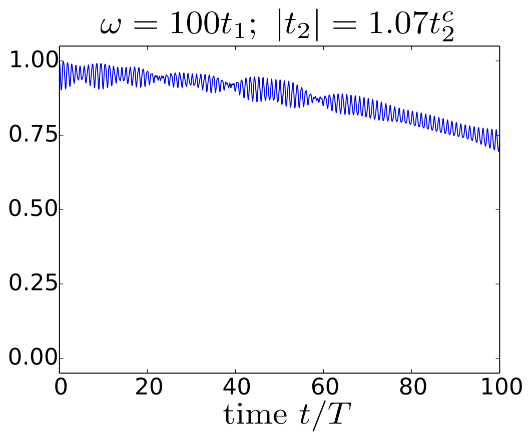

FIG. 11. Numerical measurement of the fidelity $F(t) = |\langle \Psi(t) \mid \Psi_{\mathrm{eff}}(t)\rangle|$ for the time evolution over 100 periods in the single-particle case ($U = 0$). Exact time-dependent evolution is performed for $V = \sqrt{2\omega t_2}$.

time. The total error becomes smaller when we increase the ratio ω/t_1 or decrease t_2/t_1. This effect is observed more quantitatively in Figs. 12(a) and 12(b), where we plot the fidelity for different values of parameters ω and t_2. For clarity, we do not show the entire time evolution, but only the value of $F(t)$ at few stroboscopic times. In Fig. 12(e), we also plot the diagram of minima and local intraperiodic maxima of the fidelity, corresponding to the lowest position of the "envelop" of $F(t)$.

Another important point, not captured by Floquet theory and the HFE, and which appears in simulations, is the fact that the time evolution with both effective and exact Hamiltonians depends on the initial state $|\Psi_0\rangle$. In our numerical simulations we consider three different types of initial states: the ground state of the effective Hamiltonian $|GS_{\mathrm{eff}}\rangle$, the ground state of the unperturbed Hamiltonian $|GS_0\rangle$, and a state $|\Psi_{\mathrm{rand}}\rangle$ with a random wave function.

All properties related to the fidelity, described above, are observed in the case of the state $|\Psi_{\mathrm{rand}}\rangle$. If, however, we consider the state $|GS_0\rangle$, we do not observe any noticeable time evolution. In the case of the state $|GS_{\mathrm{eff}}\rangle$ in the regime when the minimum of the lowest band is not localized at point $\mathbf{\Gamma}$, we clearly observe intraperiodic submotions of the system. However, the envelop of $F(t)$ is located close to the maximum and does not decay with time. This can be interpreted in terms of the symmetry of these states with respect to Hamiltonians. For example, if the initial state is one of two eigenstates at momentum $\boldsymbol{k} = 0$, it will always stay an eigenstate of both effective, exact time-dependent, and unperturbed Hamiltonians. Thus, we will not observe any evolution of the fidelity.

In order to prepare the basis for future investigations, we perform similar numerical tests for fidelities of the HFE in the many-body case. We are particularly interested in how the convergence of the HFE is modified by Bose-Hubbard interactions. As we already mentioned, interactions lead to highly nontrivial effects such as heating or decoherence [80–95]. In Figs. 12(c) and 12(d) we plot $F(t)$ for two different values of Un. We see that the effect of U leads to the faster decay of the fidelity.

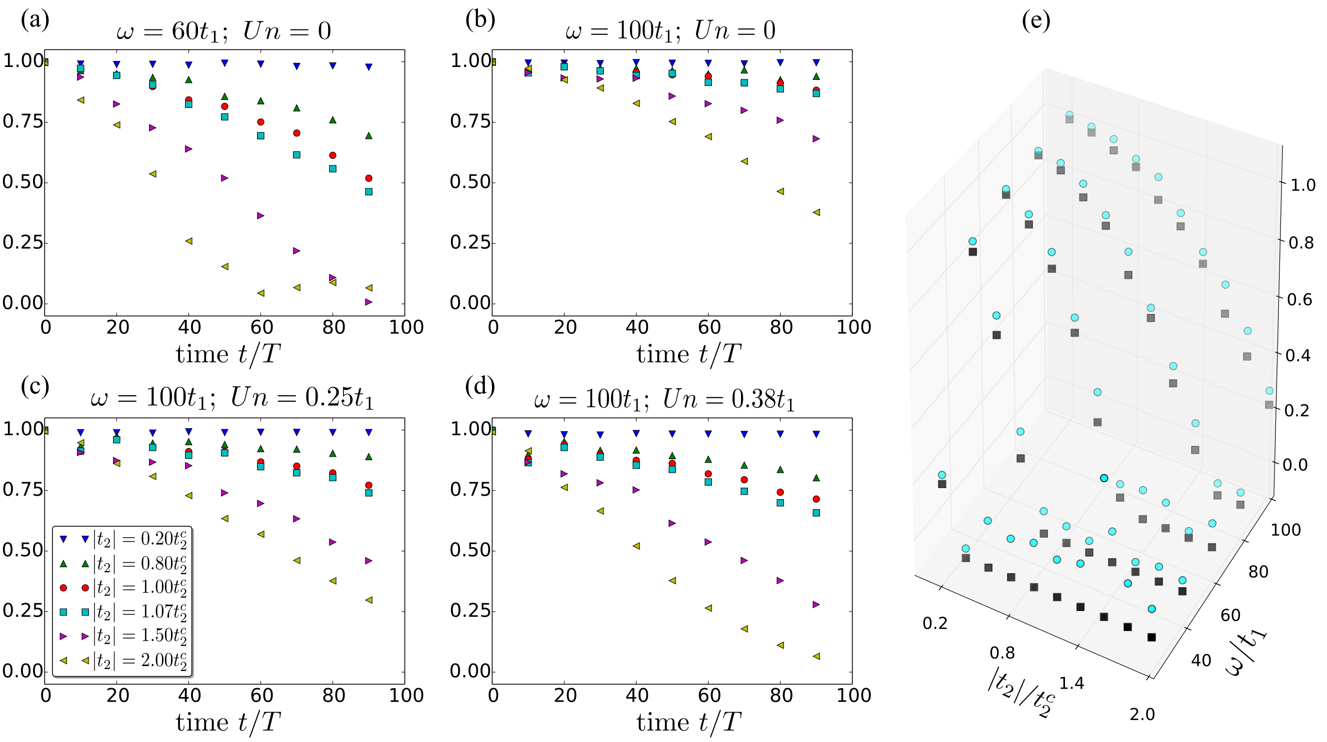

FIG. 12. Observable $F(t) = |\langle \Psi(t) \mid \Psi_{\mathrm{eff}}(t)\rangle|$ for the time evolution over $T = 100$ periods (a) and (b). Stroboscopic values of the fidelity in the single-particle case ($U = 0$) for two different values of ω. (c) and (d) Stroboscopic values of the fidelity in the many-body case for two different values of U, with $\omega = 100t_1$. (e) Diagram showing minima (black squares) and local maxima (blues circles) of $F(t)$ for different values of t_2 and ω in the single-particle case ($U = 0$). All simulations are performed with randomly distributed initial state $|\Psi_{\mathrm{rand}}\rangle$.

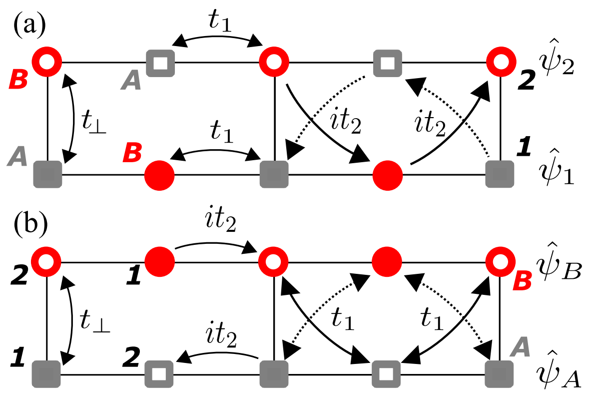

FIG. 13. Strip (ladder) geometry consisting of two coupled chains. Each site of the unit cell of this ladder is characterized by the chain index 1 or 2 (represented in the picture by the fact that the figure is either filled or not) and the sublattice index A or B (represented by the color and the shape of the figure). In the continuum limit, depending on the ratio t_1/t_2 we would prefer either to describe the system in terms of (a) operators $\hat\psi_1$ and $\hat\psi_2$ if $t_1 \gg t_2$, or (b) operators $\hat\psi_A$ and $\hat\psi_B$ if $t_1 \ll t_2$.

VI. LADDER GEOMETRY

Many theoretical and experimental works were performed during previous decades using the ladder geometry, allowing for a strip version of two-dimensional (2D) lattices and the efficient theoretical tools of quasi-one-dimensional systems such as bosonization [127–130] and numerical techniques. In particular, in bosonic systems, questions related to the Mott insulator—superfluid phase transition, effects induced by the magnetic field, such as Meissner effect, and apparition of one-dimensional (1D) equivalent of a vortex lattice [145–152] or also Laughlin bosonic phases [153] were addressed. Experimental realization of bosonic ladders, giving opportunity to study the rich and profound physics of these systems was done recently, using laser assisted tunneling [46] to create artificial gauge fields. For fermionic systems, the observation of intriguing chiral edge states in systems with synthetic dimensions was reported in Refs. [154,155], in relation to recent theoretical works [156–158]. In Ref. [159] systems of coupled Rashba nanowires subjected to a periodic time-dependent perturbation were found to support Weyl semimetal and fractional topological phases.

Motivated by this context, we consider in this section a ladder version of the anisotropic Haldane model introduced in the preceding sections (Secs. III A and IV). We reformulate the problem of Sec. IV in the ladder geometry of Fig. 13. We consider the distance between NN being equal to a. The unit cell of such ladders is formed by four distinct sites, that we will distinguish by chain index $\nu \in \{0,1\}$ and by sublattice index $c \in \{A,B\}$, with the convention that $\hat c_{\nu,i}$ is either $\hat a_{\nu,i}$ or $\hat b_{\nu,i}$, reminiscent of the 2D formulation of the problem. The effective Hamiltonian evaluated up to the first order in the HFE can be conveniently written in terms of four distinct terms $\hat H = \sum_{\nu,c} \hat H^U_{\nu,c} + \sum_\nu \hat H^{\parallel}_\nu + \sum_c \hat H^{t_2}_c + \hat H^\perp$ expressed as follows:

$$\begin{aligned}
\hat H^{\parallel}_1 + \hat H^{\parallel}_2 &= -t_1 \sum_i \big(\hat a^\dagger_{1,2i}\hat b_{1,2i+1} + \hat a^\dagger_{1,2i}\hat b_{1,2i-1} + \hat b^\dagger_{2,2i}\hat a_{2,2i+1} \\
&\quad + \hat b^\dagger_{2,2i}\hat a_{2,2i-1} + \mathrm{H.c.}\big),\\
\hat H^{t_2}_A + \hat H^{t_2}_B &= -it_2 \sum_i \big(\hat a^\dagger_{1,2i}\hat a_{2,2i+1} + \hat a^\dagger_{2,2i-1}\hat a_{1,2i} \\
&\quad + \hat b^\dagger_{2,2i}\hat b_{1,2i-1} + \hat b^\dagger_{1,2i+1}\hat b_{2,2i} - \mathrm{H.c.}\big),\\
\hat H^\perp &= -t_\perp \sum_i \big(\hat a^\dagger_{1,2i}\hat b_{2,2i} + \hat b^\dagger_{2,2i}\hat a_{1,2i}\big),\\
\hat H^U_{\nu,c} &= \frac{U}{2}\sum_i \hat n_{\nu,c,i}(\hat n_{\nu,c,i} - 1). \qquad (50)
\end{aligned}$$

in which the spatial index i runs over $[1,2,\ldots,L/2]$, with L the length of the ladder containing $L/2$ unit cells. If we compare the strip geometry to the 2D geometry, we should consider $t_\perp = t_1$. Yet, we will study a more general case with arbitrary hopping $t_\perp$.

A. Single-particle spectrum basis

We first calculate the band structure $\epsilon_0(k)$ of the noninteracting system by going to the momentum space. The Hamiltonian is rewritten in terms of 4×4 matrices $\mathcal{H}(k)$ as follows: $\hat H = -\sum_k \hat\psi^\dagger_k \cdot \mathcal{H}(k) \cdot \hat\psi_k$, where $k \in [-\frac{\pi}{2a},\frac{\pi}{2a}]$ is the vector in the 1D BZ, $\hat\psi_k = (\hat a_{1,k},\hat b_{1,k},\hat a_{2,k},\hat b_{2,k})^t$ and

$$\hat{\mathcal{H}}(k) = \begin{pmatrix} 0 & 2t_1\cos(ak) & -2t_2\sin(ak) & t_\perp \\ 2t_1\cos(ak) & 0 & 0 & 2t_2\sin(ak) \\ -2t_2\sin(ak) & 0 & 0 & 2t_1\cos(ak) \\ t_\perp & 2t_2\sin(ak) & 2t_1\cos(ak) & 0 \end{pmatrix}. \qquad (51)$$

In Fig. 14, we show the spectrum $\epsilon_0(k)$ for various t_2. If we consider, for instance, $t_2 = 0$, we find that the spectrum $\epsilon_0(k) = \pm\frac{1}{2}[t_\perp \pm \sqrt{t_\perp^2 + 16t_1^2\cos^2(ak)}]$, to be compared to the standard ladder bands $\epsilon_0(k) = \pm t_\perp - 2t_1\cos(ak)$. In the general case, the four eigenvalues of $\mathcal{H}(k)$ are

$$\epsilon_0(k) = \pm\tfrac{1}{2}\Big[t_\perp \pm \sqrt{t_\perp^2 + 16t_1^2\cos^2(ak) + 16t_2^2\sin^2(ak)}\Big]. \qquad (52)$$

From this equation and Fig. 14, we observe that there is a transition at $t_1 = t_2$, separating the situation $t_2 < t_1$, in which the minimum of the lowest band is located at $k = 0$, from the situation $t_2 > t_1$, where the minimum of the lowest band is $k = \pi/2a$ (up to a reciprocal lattice vector). This is thus analog to the ZM-FM transition of the 2D version of the model, except that the minimum at $k = \pi/2a$ does not move when changing t_2. This transition is actually related to the duality in the model, appearing in Fig. 13, in which $t_1 \leftrightarrow it_2$ and one site each two is

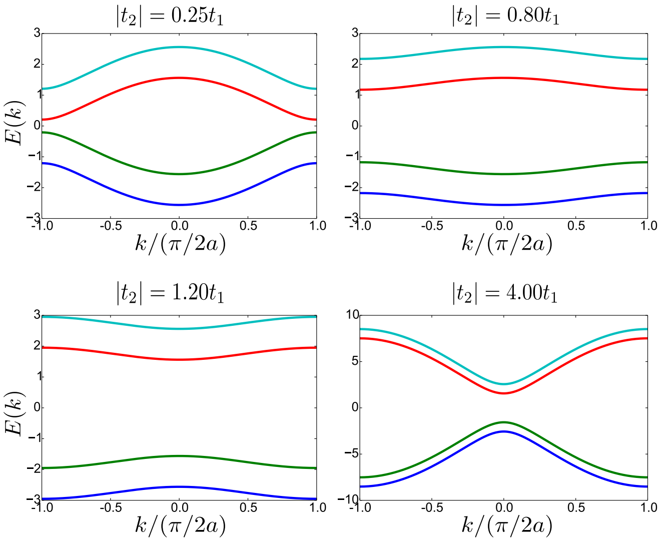

FIG. 14. Single particle spectra of the ladder model ($U = 0$). All figures have parameters $t_1 = t_\perp = 1$. We see that as t_2 increases, the minima of the bands moves from $k = 0$ to $k = \pm\frac{\pi}{2a}$. The gap between middle bands closes at $t_2 = 0$.

exchanged. This duality maps local kinetic energy onto current operators and explains the $t_1 = t_2$ transition point.

It is lastly important to notice that, at this very transition point $t_1 = t_2$, the model displays flat bands since the four energies become $\epsilon_0(k) = \pm\frac{1}{2}[t_\perp \pm \sqrt{t_\perp^2 + 16t_1^2}]$ and are thus independent of k. Such peculiar band structure makes it difficult to analyze the effect of interactions on the model and we leave this question for possible future investigations. Consequently, as bosonization requires one to linearize the bands and numerics become challenging for flat band models, we discuss in what follows the regimes $t_2 \ll t_1$ and $t_2 \gg t_1$, expecting that a third phase would appear around the transition point. This gives an account on how the two phases emerge in the presence of interactions.

B. Low energy continuum description and two competing phases

In order to describe the behavior of the interacting system in ZM and FM phases, far from the regime of flat bands, we write Hamiltonian (50) in the continuum limit. If one considers only one chain, for instance, its low-energy description falls into the universality class of Tomonaga-Luttinger liquids. Excitations are collective sound modes with linear dispersion and are described using the "harmonic fluid approach" also known as "bosonization" [127–130]. In the geometry under study and setting $x = ja$ with a the lattice spacing, one has the freedom to define either the set of operators $\hat\psi_{1(2)}(x) = \hat c_{1(2),j}/\sqrt{a}$, corresponding to the lower/upper chain prescription, or the operators $\hat\psi_{A(B)}(x) = \hat a(\hat b)_j/\sqrt{a}$ that correspond to the sublattice prescription. This choice of prescription is schematically represented in Fig. 13. Bosonic creation operators $\hat\psi_\nu^\dagger(x)$ are then written in terms of new bosonic fields $\hat\theta_\nu(x)$ and $\hat\phi_\nu(x)$ via the following relation:

$$\hat\psi_\nu^\dagger(x) = \left(\rho_0 - \frac{1}{\pi}\nabla\hat\phi_\nu(x)\right)^{1/2}\sum_p e^{i2p(\pi\rho_0 x - \hat\phi_\nu(x))}e^{-i\hat\theta_\nu(x)}. \tag{53}$$

The $\hat\theta_\nu(x)$ are phase fields and the $\hat\phi_\nu(x)$ are the long wavelength density excitation, such that $-\nabla\hat\phi_\nu(x)/\pi = \hat\rho_\nu(x) - \rho_0$, in which $\hat\rho_\nu(x)$ is the density operator and ρ_0 its mean value in the ground state. If the system is translationally invariant, $\rho_0 = n/a$ with $n = N/N_s$ the filling. Operators $\hat\theta_\nu(x)$ and $\hat\phi_\nu(x)$ satisfy the following commutation relation:

$$[\hat\phi_\mu(x),\hat\theta_\nu(x')] = i\frac{\pi}{2}\delta_{\mu\nu}\,\mathrm{Sgn}(x - x'). \tag{54}$$

The oscillating contribution in Eq. (53) reflects the ordering in the lattice description of the model (particles tend to develop a crystal-like structure). If one averages the density over the distances large compared to a, only the $p = 0$ term will remain. This is the simplification that we will consider in the following.

C. Strong t_1 phase

When NNN hopping amplitude t_2 is small compared to t_1, the lower/upper chain prescription is well suited. This allows us to express $\hat H_\nu^L = \hat H_\nu^\parallel + \hat H_{\nu,A}^U + \hat H_{\nu,B}^U$ as follows:

$$\hat H_\nu^L = \int \frac{dx}{2\pi}\left(vK|\nabla\hat\theta_\nu(x)|^2 + \frac{v}{K}|\nabla\hat\phi_\nu(x)|^2\right), \tag{55}$$

where the speed of sound is v and the Luttinger parameter is K. In the weakly interacting limit, they are identified as $v = \rho_0\sqrt{t_1 U}$ and $K = \sqrt{t_1/U}$. Furthermore, the Luttinger parameter satisfies $K > 1$ for finite repulsive short-range interactions and $K = 1$ in the hard core limit. The two chains are coupled by the following terms:

$$\hat H^\perp = -\rho_0 t_\perp \int dx\,\cos[\hat\theta_1(x) - \hat\theta_2(x)], \tag{56}$$

and

$$\begin{aligned}\hat H_A^{t_2} + \hat H_B^{t_2} = \rho_0 t_2 \int dx(&\sin[\hat\theta_2(x+a) - \hat\theta_1(x)]\\ &+ \sin[\hat\theta_1(x) - \hat\theta_2(x-a)]\\ &+ \sin[\hat\theta_2(x) - \hat\theta_1(x+a)]\\ &+ \sin[\hat\theta_1(x-a) - \hat\theta_2(x)]).\end{aligned} \tag{57}$$

If $t_\perp$ is strong (compared to t_1), phases $\hat\theta_\mu(x)$ will be pinned by the term $\hat H^\perp$ in such a way that $\langle\hat\theta_1(x)\rangle = \langle\hat\theta_2(x)\rangle = \text{const}$, where $\langle.\rangle$ is taken in the ground state. Such configuration also implies that $\langle\hat H_c^{t_2}\rangle = 0$ and bosons on two chains form a quasicondensate at the point $k = 0$ in the BZ. The expectation value of $\hat\theta_\nu(x+a) - \hat\theta_\nu(x)$ and $\hat\theta_2(x+a) - \hat\theta_1(x)$ is related to the value of densities of local currents between, respectively, NN and NNN sites. One can deduce in particular that to the lowest order in a all currents that flow in the right direction (with increasing x) can be expressed as

$$\begin{aligned}J_{AB,r}^{\parallel,1} &= -J_{AB,r}^{\parallel,2} = -2\rho_0\,\mathrm{Im}[t_1\langle e^{i(\hat\theta_1(x)-\hat\theta_1(x+a))}\rangle] = 0,\\ J_{AA,r} &= -J_{BB,r} = -2\rho_0\,\mathrm{Im}[it_2\langle e^{i(\hat\theta_1(x)-\hat\theta_2(x+a))}\rangle]\\ &= -2\rho_0 t_2.\end{aligned} \tag{58}$$

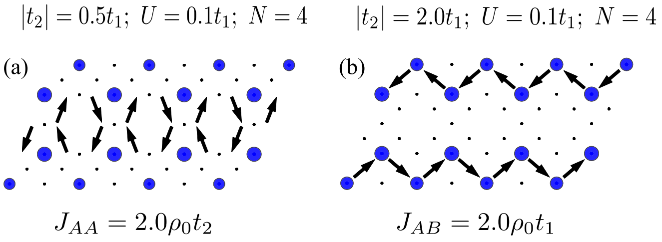

FIG. 15. Numerical simulations showing the LDOS ρ_i (via scaling of blue circles) and the lattice current density J_{ij} (black arrows) in the ground state of the system in ladder geometry with 8×2 sites. (a) The phase $t_1 > t_2$ is characterized by $|J^{\parallel}_{AB}| = 0$ and $|J_{AA}| \approx 2\rho_0 t_2$. (b) The phase $t_1 < t_2$ is characterized by $|J^{\parallel}_{AB}| \approx 2\rho_0 t_1$ and $|J_{AA}| = 0$. All simulations were performed in the system with PBC along the x axis.

Indices AB and AA correspond, respectively, to NN and NNN currents, 1 and 2 are chain indices, and r refers to the right direction. Interchain currents are zero everywhere:

$$J^{\perp}_{AB} = -2\rho_0\,\mathrm{Im}[t_1\langle e^{i(\hat{\theta}_2(x)-\hat{\theta}_1(x))}\rangle] = 0, \tag{59}$$

which is a property related to the Meissner phase in bosonic ladders, observed in particular in the experimental realization reported in Ref. [46].

We illustrate this scenario by ED calculations. The numerical results are shown in Fig. 15(a) and display the expected current pattern for $t_2 = t_1/2$.

D. Strong t_2 phase

From the other side, when t_2 is strong, terms $\hat{H}^{t_2}_A$ and $\hat{H}^{t_2}_B$ favor the generation of two decoupled intercrossing chains characterized by $\langle\hat{\theta}_2(x+a) - \hat{\theta}_1(x)\rangle = \langle\hat{\theta}_1(x) - \hat{\theta}_2(x-a)\rangle = -\pi/2$ (i.e., the phase decreases with x), and $\langle\hat{\theta}_1(x+a) - \hat{\theta}_2(x)\rangle = \langle\hat{\theta}_2(x) - \hat{\theta}_1(x-a)\rangle = \pi/2$ (i.e., the phase increases with x) for all $x = 2ja$. In order to simply describe this phase, one uses the sublattice prescription, considers operators $\hat{\theta}_{A/B}(x)$ and $\hat{\phi}_{A/B}(x)$ and performs the gauge transformation: $\hat{\theta}_{A/B}(x) \to \hat{\theta}'_{A/B}(x) = \hat{\theta}_{A/B}(x) \pm \pi x/2a$. This leads to

$$\hat{H}^{t_2}_c + \hat{H}^U_{1,c} + \hat{H}^U_{2,c} = \int \frac{dx}{2\pi}\left(uK|\nabla\hat{\theta}'_c(x)|^2 + \frac{u}{K}|\nabla\hat{\phi}_c(x)|^2\right), \tag{60}$$

with u,K the corresponding parameters. The two chains are coupled by t_1 and $t_\perp$ terms in the following way:

$$\hat{H}^{\perp} = -t_\perp\rho_0\int dx\cos[\hat{\theta}_A(x) - \hat{\theta}_B(x)], \tag{61}$$

and

$$\begin{aligned}\hat{H}^{\parallel}_1 + \hat{H}^{\parallel}_2 = -t_1\rho_0\int dx(&\cos[\hat{\theta}_B(x+a) - \hat{\theta}_A(x)]\\ &+ \cos[\hat{\theta}_A(x) - \hat{\theta}_B(x-a)]\\ &+ \cos[\hat{\theta}_B(x) - \hat{\theta}_A(x-a)]\\ &+ \cos[\hat{\theta}_A(x+a) - \hat{\theta}_B(x)]).\end{aligned} \tag{62}$$

The ground state in the strong t_2 limit corresponds to the quasicondensation of bosons at the point $k = \pm\frac{\pi}{2a}$ (defined up to a reciprocal lattice vector π/a) in the BZ. The effect of the $t_\perp$ coupling consists of pinning the phases of the two chains. One remarks that, according to the duality, t_1 plays the same role as t_2 in the strong t_1 phase. We are also interested in how expectation values of the local current are modified. Straightforward calculations imply that in the strong t_2 phase currents (expressed in the same way as previously) become

$$\begin{aligned}J^{\parallel,1}_{AB,r} &= -J^{\parallel,2}_{AB,r} = -2\rho_0\,\mathrm{Im}[t_1\langle e^{i(\hat{\theta}_1(x)-\hat{\theta}_1(x+a))}\rangle] = 2\rho_0 t_1,\\ J_{AA,r} &= -J_{BB,r} = -2\rho_0\,\mathrm{Im}[it_2\langle e^{i(\hat{\theta}_1(x)-\hat{\theta}_2(x+a))}\rangle] = 0,\\ J^{\perp}_{AB} &= -2\rho_0\,\mathrm{Im}[t_1\langle e^{i(\hat{\theta}_2(x)-\hat{\theta}_1(x))}\rangle] = 0.\end{aligned} \tag{63}$$

These analytical predictions are also illustrated by ED simulations gathered in Fig. 15(b).

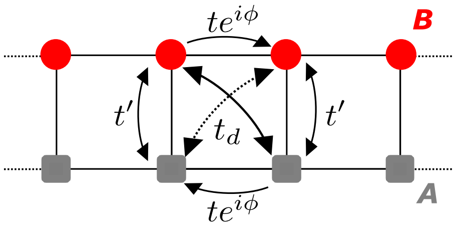

FIG. 16. Schematic representation of the ladder model of Refs. [160,161], which can be generated by using the Floquet theory and the HFE, starting from the Hamiltonian (1).

E. Related model

We emphasize that many other effective models with nontrivial profound physics could be generated using the time-dependent model described by Eq. (1). In particular, one could consider the square lattice with phases θ_{ij} distributed in the following way: $\theta_{ij} = \pi/2$ for all horizontal hoppings from the right to the left and $\theta_{ij} = 0$ for all vertical hoppings from the bottom to the top. The resulting model is geometrically equivalent to the model of Refs. [160,161] (in the last reference it was also referred to as the Creutz model) and sketched in Fig. 16. This model also possesses a one to two quantum well transition at the bosonic ground-state level and nontrivial topological properties related to the generation of an effective spin-orbit coupling (due to t_d term that couples different chains of the ladder at neighboring positions j).

VII. CONCLUSION

To summarize, we have shown exotic physics induced by Floquet modulation of lattice systems, using analytical calculations supported by exact diagonalizations. First, in relation with the realization of topological phases, we have shown how to engineer analogs of Haldane Chern insulators with anisotropic next-nearest neighbor couplings. In the context of photon systems, the ground state corresponds to the vacuum in the bulk; shining light with a frequency within the gap between the Bloch bands would allow one to realize one-way motion of light at the edges, thereby probing the topological nature [31,32,34]. Then, focusing on the s band of an optical lattice, we have shown how to engineer a BEC analog of a FFLO state, usually predicted for fermionic systems within

Bardeen-Cooper-Schrieffer theory. The transition can be detected via an indirect measurement of Meissner currents along NNNs, averaged over one period of the Floquet perturbation, or by focusing on the momentum distribution of bosons. We find that the nature of the QPT is different in the isotropic [53] and anisotropic contexts. In the latter case studied in the present paper, the transition is of second-order type, which is exemplified by the continuity of Chiral currents at the transition. Closed loops of Chiral currents also involve lozenges instead of triangles. We have shown how interactions affect the band structure and the momentum distribution across the QPT. The effect of quite large interactions on the Floquet theory leading potentially to heating and decoherence effects will be studied separately. The present engineered gauge for the vector potentials also allows tractable solutions in ladder (strip) geometries. We have shown, using bosonization and exact diagonalization, that a similar chiral bosonic QPT occurs in this case. However, the vicinity of the phase transition, which exhibits flat bands, is more complex and it will consequently be studied separately. Similar Meissner currents have already been reported in bosonic ladders [46] by analogy to superconductors. This time-dependent approach could also be extended to simulate spin-orbit models in relation with iridate materials [9,140,162,163].

ACKNOWLEDGMENTS

This work has benefited from discussions and collaborations with Ivana Vasic, Alexandru Petrescu, and Walter Hofstetter. We also acknowledge discussions with Immanuel Bloch, Benoît Douçot, Tianhan Liu, Belen Paredes, Arun Paramekanti, Leticia Tarruell, Ronny Thomale, Julien Gabelli, Jérome Estève, Loïc Herviou, Loïc Henriet, and Aleksey Fedorov. We acknowledge discussions at CIFAR meetings in Canada and at conferences in University of Cergy-Pontoise. We acknowledge support from the German Science Foundation (DFG) FOR2414. We also acknowledge support from the PALM Labex, Paris-Saclay, Grant No. ANR-10-LABX-0039.

APPENDIX A: EFFECTIVE HALDANE HAMILTONIAN AND DOMINANT TERMS IN DYSON SERIES FOR OBSERVABLES

It is known that the Floquet Hamiltonian obtained through the Floquet-Magnus expansion is related to the Dyson series [137] and the (general) time-dependent perturbation theory [67]. In this appendix, we emphasize this point, by showing the similarity between observables calculated in the context of time-dependent perturbation theory and with the effective Hamiltonian in the context of the HFE, by considering the particular case of the anisotropic Haldane model.

1. Perturbation theory

We consider the system evolving with the Hamiltonian $\hat{H}(t) = \hat{H}_0 + \hat{V}(t)$ and we treat the time-dependent term perturbatively. We now define the operator,

$$\hat{S}(t,t_0) = e^{iH_0(t-t_0)}\hat{U}(t,t_0), \tag{A1}$$

where

$$\hat{U}(t,t_0) = \mathcal{T}\exp\left[-i\int_{t_0}^{t} dt_1 \hat{H}(t_1)\right] \tag{A2}$$

is the evolution operator and $\mathcal{T}$ the time-ordered product. One easily obtains that

$$\hat{S}(t,t_0) = \mathcal{T}\exp\left[-i\int_{t_0}^{t} dt_1 \hat{V}_I(t_1,t_0)\right], \tag{A3}$$

where $\hat{A}_I(t,t_0)$ is the operator in the interaction picture: $\hat{A}_I(t,t_0) = e^{i\hat{H}_0(t-t_0)}\hat{A}(t)e^{-i\hat{H}_0(t-t_0)}$. We consider that the argument in the exponential in Eq. (A3) is small. We thus expand the exponential in the Dyson series and calculate the time-ordered product:

$$\begin{aligned}\hat{S}(t,t_0) = 1 &- i\int_{t_0}^{t} \hat{V}_I(t_1,t_0)dt_1 \\ &- \int_{t_0}^{t} dt_1 \int_{t_0}^{t_1} dt_2 \hat{V}_I(t_1,t_0)\hat{V}_I(t_2,t_0) + \cdots .\end{aligned} \tag{A4}$$

When the system is initially prepared in state $|\phi(t=0)\rangle = |\phi_0\rangle$, the mean value of an observable O at time t reads

$$O(t) = \langle \hat{O}(t)\rangle_t = \langle\phi_0|\, \hat{S}^\dagger(t,t_0)\hat{O}_I(t,t_0)\hat{S}(t,t_0)\, |\phi_0\rangle . \tag{A5}$$

This provides an expansion of $O(t)$ and study of the first contributions in the following.

2. Observables

a. Second-neighbor currents

The continuity equation in the Schrödinger picture for the particle density $n_{A,i}$ at site i on sublattice A takes the form,

$$\frac{d\,\langle \hat{n}_{A,i}\rangle_t}{dt} = \frac{d}{dt}\,\langle\phi(t)|\, \hat{n}_{A,i}\, |\phi(t)\rangle = -\,\langle \hat{J}_{A,i}(t)\rangle_t . \tag{A6}$$

The operator $\hat{J}_{A,i}(t)$ represents the sum of local instantaneous currents at the corresponding site. When the system is out of equilibrium, these currents do not vanish in general. By performing the calculation of the commutator, we immediately obtain

$$\hat{J}_{A,i}(t) = i\sum_{j(i)}[-t_1 + V\cos(\omega t + \theta_{ij})](\hat{a}_i^\dagger\hat{b}_j - \hat{b}_j^\dagger\hat{a}_i), \tag{A7}$$

where $\sum_{j(i)}$ denotes the sum over all sites j, NN of a given site i.

After some calculations, one gets that the first nontrivial term, that does not vanish when integrated over an integer number of periods, appears at first order in the Dyson expansion as follows:

$$J^{(2)}_{A,i}(t) = \left\langle i\left[\int_{t_0}^{t} dt_1 \hat{V}_I(t_1,t), \hat{J}^{(1)}_{A,i}(t)\right]\right\rangle_{t,0}, \tag{A8}$$

where $\langle\cdots\rangle_{t,0} = \langle\phi_0|e^{i\hat{H}_0(t-t_0)}(\cdots)e^{-i\hat{H}_0(t-t_0)}|\phi_0\rangle$. Now we want to take into account the fact that ω is the largest energy scale in the system. We perform the integration over time and neglect all subdominant order terms in $1/\omega^2$.

We obtain

$$J^{(2)}_{A,i}(t) \approx -\frac{V^2}{\omega}\left[\sum_{j(i),l(i)} \cos(\omega t+\theta_{ij})\sin(\omega t+\theta_{il})\,\langle \hat{b}_j^\dagger \hat{b}_l + \hat{b}_l^\dagger \hat{b}_j\rangle_{t,0} - \sum_{\langle\langle k|i\rangle\rangle}\cos(\omega t+\theta_{ij})\sin(\omega t+\theta_{kj})\,\langle \hat{a}_i^\dagger \hat{a}_k+\hat{a}_k^\dagger \hat{a}_i\rangle_{t,0}\right]. \quad \text{(A9)}$$

We notice that the first term is odd under the change $j \to l$ and that j is fixed by the choice of i and k in the second term. We are interested in calculating the average of $J^{(2)}_{A,i}(t)$ over the period T. After some calculations this leads to

$$\int_{t_0}^{t_0+T} dt \frac{d\,\langle \hat{n}_{A,i}\rangle_t}{dt} = \frac{V^2}{2\omega}\sum_{\langle\langle k|i\rangle\rangle}\sin(\Theta_{ik})\int_{t_0}^{t_0+T} dt\,\langle \hat{a}_i^\dagger \hat{a}_k + \hat{a}_k^\dagger \hat{a}_i\rangle_{t,0}. \quad \text{(A10)}$$

Here $\Theta_{ik} = \theta_{ij} + \theta_{jk}$ for any NNN sites i and k on the sublattice A with the same NN site j on the sublattice B. The first term has dropped in the expression because of the sign under the exchange $j \to l$. Last, we notice that we recover the expression of the $t_{2,ik}$ hopping amplitude found in the HFE.

Finally, we see that these averaged currents are almost the same as the ones obtained from the effective Hamiltonian. The only difference is that effective currents are calculated in the state evolving with the complete effective Hamiltonian $\hat{H}_{\text{eff}}$, in which case we take the average $\langle\cdots\rangle_t$, while averaged currents are calculated in the state evolving with $\hat{H}_0$, in which case the average is $\langle\cdots\rangle_{t,0}$:

$$\frac{d\left\langle \hat{n}^{\text{eff}}_{A,i}\right\rangle_t}{dt} = -\,i\left\langle\left[\hat{n}_{A,i},\hat{H}^{(1)}_{\text{eff}}\right]\right\rangle_t = \frac{V^2}{2\omega}\sum_{\langle\langle k|i\rangle\rangle}\sin(\Theta_{ik})\,\langle \hat{a}_i^\dagger \hat{a}_k + \hat{a}_k^\dagger \hat{a}_i\rangle_t. \quad \text{(A11)}$$

b. Displacement of the momentum distribution

The variation of the momentum distribution $n_{\mathbf{k}}$ is closely (but not directly) related to the form of currents expressed in the previous subsection. In the initial state, the momentum distribution is likely to be peaked at $\mathbf{k} = 0$ so observing an FM condensate requires that $n_{\mathbf{k}}$ evolves significantly in time. More precisely, we have on sublattice A the contribution,

$$\frac{d\,\langle \hat{n}_{A,\mathbf{k}}\rangle_t}{dt} = \frac{1}{N_c}\sum_i\left(\frac{d\,\langle \hat{n}_{A,i}\rangle_t}{dt} + \sum_{j\neq i} e^{i\mathbf{k}(\mathbf{r}_i-\mathbf{r}_j)}\frac{d\,\langle \hat{a}_i^\dagger \hat{a}_j\rangle_t}{dt}\right). \quad \text{(A12)}$$

Thanks to the fact that effective NNN currents should be conserved, one can argue that the first term in the expression above should sum up to zero when integrated over the full period of time T.

In order to calculate the effect of the second term, we need to perform the power expansion of $d\,\langle \hat{a}_i^\dagger \hat{a}_j\rangle_t/dt$ at the same order as $d\langle \hat{n}_{A,i}\rangle_t/dt$. We see that despite the more complicated dependency on the on-site creation and annihilation operators $\hat{a}_i^\dagger(\hat{b}_i^\dagger)$ and $\hat{a}_i(\hat{b}_i)$ (containing terms of currents between second- and fourth-nearest neighbors), this term will have exactly the same time dependency through the factor,

$$\frac{V^2}{\omega}\sum_{\langle\langle p|j\rangle\rangle}[\cos(\omega t+\theta_{jk})\sin(\omega t+\theta_{pk})]\,\langle \hat{a}_p^\dagger \hat{a}_i + \hat{a}_i^\dagger \hat{a}_p\rangle_{t,0}. \quad \text{(A13)}$$

When integrated over the full period of time, this factor will become an odd function of $\Theta_{jp} = \theta_{jk} + \theta_{kp}$, which sums up to zero inside the summation $\sum_{i<j}$. Thus, we conclude that in the regime of weak perturbation, we should have

$$\int_{t_0}^{t_0+T} dt\frac{d\,\langle \hat{n}_{A,\mathbf{k}}\rangle_t}{dt} = 0, \quad \text{(A14)}$$

up to the order $(V/\omega)^2$, irrelevant in the regime $\omega \to \infty$.

c. Momentum distribution

In the same way one can use the Dyson series to calculate the expectation value of the momentum distribution $\hat{n}_{A,\mathbf{k}}$. In this case, the first nontrivial term, which does not vanish after taking the integration over an integer number of periods, appears only in the second order in the expansion. It is written as follows:

$$n^{(2)}_{A,\mathbf{k}}(t) = -\left\langle \int_{t_0}^{t} dt_1 \int_{t_0}^{t_1} dt_2 \{\hat{V}_I(t_1,t)\hat{V}_I(t_2,t),\hat{n}_{A,\mathbf{k}}\}\right\rangle_{t,0} + \left\langle\left[\int_{t_0}^{t} dt_1\,\hat{V}_I(t_1,t)\right]\hat{n}_{A,\mathbf{k}}\left[\int_{t_0}^{t} dt_1\,\hat{V}_I(t_1,t)\right]\right\rangle_{t,0}, \quad \text{(A15)}$$

with $\{,\}$ the anticommutator. One easily sees that different terms in the expression contribute as $(V/\omega)^2$, that is $1/\omega$ times smaller than the biggest contribution for currents:

$$\langle \hat{n}_{A,\mathbf{k}}\rangle_t = \langle \hat{n}_{A,\mathbf{k}}\rangle_{t,0} + \frac{1}{\omega}\frac{V^2}{\omega}(\cdots). \quad \text{(A16)}$$

We conclude that the momentum distribution is not the most convenient observable to be studied in the weak perturbation regime since it does not show any effect. Yet, the time-dependent perturbation theory is not suitable to study the regime when the perturbation becomes strong, which is the usual one in our Floquet scheme.

APPENDIX B: FM PHASE IN THE INTERMEDIATE REGIME

We recall the approximation based on the consideration of the two-well structure, which we made in order to rewrite the Hamiltonian (14) in the intermediate regime of the FM phase:

$$\hat{a}_i \approx \frac{e^{-i\boldsymbol{K}_c\boldsymbol{r}_i}\hat{a}_{\boldsymbol{K}_c} + e^{i\boldsymbol{K}_c\boldsymbol{r}_i}\hat{a}_{-\boldsymbol{K}_c}}{\sqrt{N_c}},$$

$$\hat{b}_i \approx \frac{e^{-i\boldsymbol{K}_c\boldsymbol{r}_i}\hat{b}_{\boldsymbol{K}_c} + e^{i\boldsymbol{K}_c\boldsymbol{r}_i}\hat{b}_{-\boldsymbol{K}_c}}{\sqrt{N_c}}. \quad \text{(B1)}$$

By using this, we obtain the most general approximation of the Hamiltonian:

$$
\begin{aligned}
\hat{H} \approx{}& \epsilon_0 N - 4t_2 \sin\left(z_c\frac{\pi}{2}\right)\sum_{\mu=\pm}\mu\left(\hat{a}^\dagger_{\mu\boldsymbol{K}_c}\hat{a}_{\mu\boldsymbol{K}_c} - \hat{b}^\dagger_{\mu\boldsymbol{K}_c}\hat{b}_{\mu\boldsymbol{K}_c}\right) - t_1\left[2\cos\left(\frac{\pi z_c}{2}\right)+1\right]\sum_{\mu=\pm}\left(\hat{a}^\dagger_{\mu\boldsymbol{K}_c}\hat{b}_{\mu\boldsymbol{K}_c} + \text{H.c.}\right)\\
&+\frac{U}{2}\sum_{\mu=\pm}\left[\hat{a}^\dagger_{\mu\boldsymbol{K}_c}\hat{a}_{\mu\boldsymbol{K}_c}\left(\frac{\hat{a}^\dagger_{\boldsymbol{K}_c}\hat{a}_{\boldsymbol{K}_c}+\hat{a}^\dagger_{-\boldsymbol{K}_c}\hat{a}_{-\boldsymbol{K}_c}}{N_c}-1\right)+\hat{b}^\dagger_{\mu\boldsymbol{K}_c}\hat{b}_{\mu\boldsymbol{K}_c}\left(\frac{\hat{b}^\dagger_{\boldsymbol{K}_c}\hat{b}_{\boldsymbol{K}_c}+\hat{b}^\dagger_{-\boldsymbol{K}_c}\hat{b}_{-\boldsymbol{K}_c}}{N_c}-1\right)\right]\\
&+\frac{U}{N_s}\left[\left(\hat{a}^\dagger_{\boldsymbol{K}_c}\hat{a}_{-\boldsymbol{K}_c}\right)\left(\hat{a}^\dagger_{-\boldsymbol{K}_c}\hat{a}_{\boldsymbol{K}_c}\right)+\left(\hat{b}^\dagger_{\boldsymbol{K}_c}\hat{b}_{-\boldsymbol{K}_c}\right)\left(\hat{b}^\dagger_{-\boldsymbol{K}_c}\hat{b}_{\boldsymbol{K}_c}\right)+\text{H.c.}\right].
\end{aligned}
\tag{B2}
$$

For the incoming purpose we define

$$
\langle\hat{a}_{\pm\boldsymbol{K}_c}\rangle = \sqrt{N_{A,\pm}}e^{i\theta_{A,\pm}},\quad \langle\hat{b}_{\pm\boldsymbol{K}_c}\rangle = \sqrt{N_{B,\pm}}e^{i\theta_{B,\pm}},
\tag{B3}
$$

such that $N_{A,+}+N_{A,-}=N_A$, $N_{B,+}+N_{B,-}=N_B$, $N_{A,\pm}+N_{B,\pm}=N_\pm$, and $N_A+N_B=N_++N_-=N$. We notice that in the regime of two decoupled sublattices $t_2 \gg t_1$ one can simply write $N_{A,-}=N_{B,+}=0$. Finally, we get the expression of the GS energy E_{GS} and currents $J_{AA,\boldsymbol{v}_j}$ in terms of these new quantities:

$$
\begin{aligned}
E_{GS} ={}& \epsilon_0 N - 4t_2\sin\left(z_c\frac{\pi}{2}\right)\sum_{\mu=\pm}\mu(N_{A,\mu}-N_{B,\mu}) - 2t_1\left[2\cos\left(\frac{\pi z_c}{2}\right)+1\right]\sum_{\mu=\pm}\sqrt{N_{A,\mu}N_{B,\mu}}\cos(\theta_{B,\mu}-\theta_{A,\mu})\\
&+\frac{U}{2}\left[N_A\left(\frac{N_A}{N_c}-1\right)+N_B\left(\frac{N_B}{N_c}-1\right)\right]+\frac{U}{N_c}(N_{A,+}N_{A,-}+N_{B,+}N_{B,-}),
\end{aligned}
\tag{B4}
$$

$$
J_{AA,\boldsymbol{v}_1} = J_{AA,\boldsymbol{v}_2} = -t_2\frac{N_A}{N_c}\cos\left(z_c\frac{\pi}{2}\right),\quad J_{AA,\boldsymbol{v}_3}=0.
\tag{B5}
$$

We see that the t_1 term pins to zero the difference between phases $\theta_{B,+}-\theta_{A,+}$ and $\theta_{B,-}-\theta_{A,-}$. However, we are still free to chose separately phases $\theta_+=\theta_{A,+}=\theta_{B,+}$ and $\theta_-=\theta_{A,-}=\theta_{B,-}$, which corresponds again to the presence of two Goldstone modes.

We assume that the effect of interactions is weak enough so that we use the assumptions of Eq. (39), i.e., that the two-well structure of the system is preserved. We, however, allow for the fact that interactions can change the value of z_c and modify the position of two minima at $\pm\boldsymbol{K}_c$. In order to study in more detail this effect, we use the relations between operators $\hat{a}^\dagger_{\boldsymbol{K}_c}$ and $\hat{a}^\dagger_{-\boldsymbol{K}_c}$, based on properties of the unitary transformation (42), and write the GS energy in terms of N, N_+, $N_-=N-N_+$, and z_c only:

$$
\begin{aligned}
E_{\text{GS}} ={}& N\left\{\epsilon_0 - 4t_2\sin\left(z_c\frac{\pi}{2}\right)\frac{Y(z_c)}{\sqrt{X^2(z_c)+Y^2(z_c)}} - t_1\left[2\cos\left(z_c\frac{\pi}{2}\right)+1\right]\frac{X(z_c)}{\sqrt{X^2(z_c)+Y^2(z_c)}}\right\}\\
&+UN\left[\frac{n}{2}+\frac{Y^2(z_c)}{X^2(z_c)+Y^2(z_c)}\frac{n}{2}-\frac{1}{2}\right]+U\left[\frac{N_+(N-N_+)}{N_s}\right]\left[\frac{X^2(z_c)-2Y^2(z_c)}{X^2(z_c)+Y^2(z_c)}\right],
\end{aligned}
\tag{B6}
$$

where $X(z_c)$ and $Y(z_c)$ are defined as follows:

$$
X(z_c) = t_1\left[1+2\cos\left(z_c\frac{\pi}{2}\right)\right],\quad Y(z_c) = 4t_2\sin\left(z_c\frac{\pi}{2}\right).
\tag{B7}
$$

The first effect of interactions in the FM consists of imposing constraints on the distribution of particles in two wells N_+ and N_-. There are two distinct subregimes of the FM phase: For $t_2^c < t_2 < \sqrt{(17+\sqrt{97})/24}\,t_2^c$ the last term in Eq. (B6) is positive and interactions force all particles to chose one particular well, such that N_+ or N_- becomes precisely equal to N. At the other side, for $t_2 > \sqrt{(17+\sqrt{97})/24}\,t_2^c$ the last term in Eq. (B6) is negative and the uniform distribution of particles $N_+=N_-=N/2$ is preferred. The second effect of interactions consists of moving the position of minima at $\pm\boldsymbol{K}_c$. The contribution of interactions to the GS energy close to the transition is

$$
\Delta E'_{\text{GS}} = NUn\frac{8t_2^2}{9t_1^2}\left(z_c\frac{\pi}{2}\right)^2 + N\frac{Un}{2}\left[\frac{16}{27}\left(\frac{t_2}{t_1}\right)^2-\frac{256}{81}\left(\frac{t_2}{t_1}\right)^4\right]\left(z_c\frac{\pi}{2}\right)^4.
\tag{B8}
$$

If particles are not all located in one well, there appears an additional contribution,

$$
\Delta E''_{\text{GS}} = -\frac{16U}{3}\frac{N_+(N-N_+)}{N_s}\left(\frac{t_2}{t_1}\right)^2\left(z_c\frac{\pi}{2}\right)^2 - \frac{16U}{27}\frac{N_+(N-N_+)}{N_s}\left(\frac{3t_1^2t_2^2-16t_2^4}{t_1^4}\right)\left(z_c\frac{\pi}{2}\right)^4.
\tag{B9}
$$

The second contribution $\Delta E''_{\mathrm{GS}}$ dominates when $N_+ = N_- = N/2$, resulting in the generation of an effective repulsion between two wells.

[1] K. v. Klitzing, G. Dorda, and M. Pepper, New Method for High-Accuracy Determination of the Fine-Structure Constant Based on Quantized Hall Resistance, Phys. Rev. Lett. **45**, 494 (1980).

[2] D. C. Tsui, H. L. Stormer, and A. C. Gossard, Two-Dimensional Magnetotransport in the Extreme Quantum Limit, Phys. Rev. Lett. **48**, 1559 (1982).

[3] R. B. Laughlin, Quantized Hall conductivity in two dimensions, Phys. Rev. B **23**, 5632 (1981).

[4] F. D. M. Haldane, Nonlinear Field Theory of Large-Spin Heisenberg Antiferromagnets: Semiclassically Quantized Solitons of the One-Dimensional Easy-Axis Néel State, Phys. Rev. Lett. **50**, 1153 (1983).

[5] I. Affleck and F. D. M. Haldane, Critical theory of quantum spin chains, Phys. Rev. B **36**, 5291 (1987).

[6] I. Affleck, Quantum spin chains and the haldane gap, Journal of Physics: Condensed Matter **1**, 3047 (1989).

[7] X. Chen, Z.-C. Gu, Z.-X. Liu, and X.-G. Wen, Symmetry protected topological orders and the group cohomology of their symmetry group, Phys. Rev. B **87**, 155114 (2013).

[8] T. Senthil, Symmetry-protected topological phases of quantum matter, Annual Review of Condensed Matter Physics **6**, 299 (2015).

[9] C. L. Kane and E. J. Mele, Z_2 Topological Order and the Quantum Spin Hall Effect, Phys. Rev. Lett. **95**, 146802 (2005).

[10] M. König, S. Wiedmann, C. Brüne, A. Roth, H. Buhmann, L. W. Molenkamp, X.-L. Qi, and S.-C. Zhang, Quantum spin Hall insulator state in HgTe quantum wells, Science **318**, 766 (2007).

[11] M. Z. Hasan and C. L. Kane, Colloquium: Topological insulators, Rev. Mod. Phys. **82**, 3045 (2010).

[12] X.-L. Qi and S.-C. Zhang, Topological insulators and superconductors, Rev. Mod. Phys. **83**, 1057 (2011).

[13] M. Fruchart and D. Carpentier, An introduction to topological insulators, C. R. Phys. **14**, 779 (2013).

[14] B. A. Bernevig and T. L. Hughes, *Topological Insulators and Topological Superconductors*, STU–student edition ed. (Princeton University Press, Princeton, 2013).

[15] J. Dalibard, F. Gerbier, G. Juzeliūnas, and P. Öhberg, Colloquium: Artificial gauge potentials for neutral atoms, Rev. Mod. Phys. **83**, 1523 (2011).

[16] N. Goldman, G. Juzeliūnas, P. Öhberg, and I. B. Spielman, Light-induced gauge fields for ultracold atoms, Rep. Prog. Phys. **77**, 126401 (2014).

[17] N. Goldman, J. C. Budich, and P. Zoller, Topological quantum matter with ultracold gases in optical lattices, Nat. Phys. **12**, 639 (2016).

[18] I. Carusotto and C. Ciuti, Quantum fluids of light, Rev. Mod. Phys. **85**, 299 (2013).

[19] L. Lu, J. D. Joannopoulos, and M. Soljacic, Topological photonics, Nat. Photon. **8**, 821 (2014).

[20] K. Le Hur, L. Henriet, A. Petrescu, K. Plekhanov, G. Roux, and M. Schiró, Many-body quantum electrodynamics networks: Non-equilibrium condensed matter physics with light, C. R. Physique **17**, 808 (2016).

[21] M. J. Hartmann, Quantum simulation with interacting photons, J. Opt. **18**, 104005 (2016).

[22] P. G. Harper, Single Band Motion of Conduction Electrons in a Uniform Magnetic Field, Proc. Phys. Soc. A **68**, 874 (1955).

[23] D. R. Hofstadter, Energy levels and wave functions of Bloch electrons in rational and irrational magnetic fields, Phys. Rev. B **14**, 2239 (1976).

[24] M. Aidelsburger, M. Atala, S. Nascimbène, S. Trotzky, Y.-A. Chen, and I. Bloch, Experimental Realization of Strong Effective Magnetic Fields in an Optical Lattice, Phys. Rev. Lett. **107**, 255301 (2011).

[25] M. Aidelsburger, M. Atala, M. Lohse, J. T. Barreiro, B. Paredes, and I. Bloch, Realization of the Hofstadter Hamiltonian with Ultracold Atoms in Optical Lattices, Phys. Rev. Lett. **111**, 185301 (2013).

[26] H. Miyake, G. A. Siviloglou, C. J. Kennedy, W. C. Burton, and W. Ketterle, Realizing the Harper Hamiltonian with Laser-Assisted Tunneling in Optical Lattices, Phys. Rev. Lett. **111**, 185302 (2013).

[27] M. Aidelsburger, M. Lohse, C. Schweizer, M. Atala, J. T. Barreiro, S. Nascimbene, N. R. Cooper, I. Bloch, and N. Goldman, Measuring the Chern number of Hofstadter bands with ultracold bosonic atoms, Nat. Phys. **11**, 162 (2015).

[28] D. Jaksch and P. Zoller, Creation of effective magnetic fields in optical lattices: the Hofstadter butterfly for cold neutral atoms, New J. Phys. **5**, 56 (2003).

[29] F. D. M. Haldane and S. Raghu, Possible Realization of Directional Optical Waveguides in Photonic Crystals with Broken Time-Reversal Symmetry, Phys. Rev. Lett. **100**, 013904 (2008).

[30] S. Raghu and F. D. M. Haldane, Analogs of quantum-Hall-effect edge states in photonic crystals, Phys. Rev. A **78**, 033834 (2008).

[31] Z. Wang, Y. Chong, J. D. Joannopoulos, and M. Soljacic, Observation of unidirectional backscattering-immune topological electromagnetic states, Nature (London) **461**, 772 (2009).

[32] M. Hafezi, S. Mittal, J. Fan, A. Migdall, and J. Taylor, Imaging topological edge states in silicon photonics, Nat. Photon. **7**, 1001 (2013).

[33] F. D. M. Haldane, Model for a Quantum Hall Effect without Landau Levels: Condensed-Matter Realization of the "Parity Anomaly, Phys. Rev. Lett. **61**, 2015 (1988).

[34] M. C. Rechtsman, J. M. Zeuner, Y. Plotnik, Y. Lumer, D. Podolsky, F. Dreisow, S. Nolte, M. Segev, and A. Szameit, Photonic floquet topological insulators, Nature (London) **496**, 196 (2013).

[35] G. Jotzu, M. Messer, R. Desbuquois, M. Lebrat, T. Uehlinger, D. Greif, and T. Esslinger, Experimental realization of the topological Haldane model with ultracold fermions, Nature **515**, 237 (2014).

[36] P. Soltan-Panahi, J. Struck, P. Hauke, A. Bick, W. Plenkers, G. Meineke, C. Becker, P. Windpassinger, M. Lewenstein, and K.

Sengstock, Multi-component quantum gases in spin-dependent hexagonal lattices, Nat. Phys. **7**, 434 (2011).
[37] L. Tarruell, D. Greif, T. Uehlinger, G. Jotzu, and T. Esslinger, Creating, moving and merging dirac points with a fermi gas in a tunable honeycomb lattice, Nature (London) **483**, 302 (2012).
[38] C.-Z. Chang, J. Zhang, X. Feng, J. Shen, Z. Zhang, M. Guo, K. Li, Y. Ou, P. Wei, L.-L. Wang, Z.-Q. Ji, Y. Feng, S. Ji, X. Chen, J. Jia, X. Dai, Z. Fang, S.-C. Zhang, K. He, Y. Wang, L. Lu, X.-C. Ma, and Q.-K. Xue, Experimental observation of the quantum anomalous Hall effect in a magnetic topological insulator, Science **340**, 167 (2013).
[39] J. Wang, B. Lian, and S.-C. Zhang, Quantum anomalous Hall effect in magnetic topological insulators, Phys. Scr. **2015**, 014003 (2015).
[40] C.-X. Liu, S.-C. Zhang, and X.-L. Qi, The quantum anomalous Hall effect, arXiv:1508.07106.
[41] N. Fläschner, B. S. Rem, M. Tarnowski, D. Vogel, D.-S. Lühmann, K. Sengstock, and C. Weitenberg, Experimental reconstruction of the Berry curvature in a Floquet Bloch band, Science **352**, 1091 (2016).
[42] A. Amo, J. Lefrere, S. Pigeon, C. Adrados, C. Ciuti, I. Carusotto, R. Houdre, E. Giacobino, and A. Bramati, Superfluidity of polaritons in semiconductor microcavities, Nat. Phys. **5**, 805 (2009).
[43] J. Klaers, J. Schmitt, F. Vewinger, and M. Weitz, Bose-Einstein condensation of photons in an optical microcavity, Nature (London) **468**, 545 (2010).
[44] J. Struck, C. Ölschläger, M. Weinberg, P. Hauke, J. Simonet, A. Eckardt, M. Lewenstein, K. Sengstock, and P. Windpassinger, Tunable Gauge Potential for Neutral and Spinless Particles in Driven Optical Lattices, Phys. Rev. Lett. **108**, 225304 (2012).
[45] K. Jiménez-García, L. J. LeBlanc, R. A. Williams, M. C. Beeler, A. R. Perry, and I. B. Spielman, Peierls Substitution in an Engineered Lattice Potential, Phys. Rev. Lett. **108**, 225303 (2012).
[46] M. Atala, M. Aidelsburger, M. Lohse, J. T. Barreiro, B. Paredes, and I. Bloch, Observation of chiral currents with ultracold atoms in bosonic ladders, Nat. Phys. **10**, 588 (2014).
[47] J. Struck, C. Ölschläger, R. Le Targat, P. Soltan-Panahi, A. Eckardt, M. Lewenstein, P. Windpassinger, and K. Sengstock, Quantum simulation of frustrated classical magnetism in triangular optical lattices, Science **333**, 996 (2011).
[48] J. Struck, M. Weinberg, C. Olschlager, P. Windpassinger, J. Simonet, K. Sengstock, R. Hoppner, P. Hauke, A. Eckardt, M. Lewenstein, and L. Mathey, Engineering Ising-XY spin-models in a triangular lattice using tunable artificial gauge fields, Nat. Phys. **9**, 738 (2013).
[49] C. J. Kennedy, W. C. Burton, W. C. Chung, and W. Ketterle, Observation of Bose-Einstein condensation in a strong synthetic magnetic field, Nat. Phys. **11**, 859 (2015).
[50] L.-K. Lim, A. Hemmerich, and C. M. Smith, Artificial staggered magnetic field for ultracold atoms in optical lattices, Phys. Rev. A **81**, 023404 (2010).
[51] G. Möller and N. R. Cooper, Condensed ground states of frustrated Bose-Hubbard models, Phys. Rev. A **82**, 063625 (2010).
[52] M. P. Zaletel, S. A. Parameswaran, A. Rüegg, and E. Altman, Chiral bosonic Mott insulator on the frustrated triangular lattice, Phys. Rev. B **89**, 155142 (2014).
[53] I. Vasic, A. Petrescu, K. Le Hur, and W. Hofstetter, Chiral bosonic phases on the Haldane honeycomb lattice, Phys. Rev. B **91**, 094502 (2015).
[54] P. Fulde and R. A. Ferrell, Superconductivity in a strong spin-exchange field, Phys. Rev. **135**, A550 (1964).
[55] A. Larkin and Y. Ovchinnikov, Nonuniform state of superconductors, Sov. Phys. JETP **20**, 762 (1964).
[56] A. Isacsson and S. M. Girvin, Multiflavor bosonic Hubbard models in the first excited Bloch band of an optical lattice, Phys. Rev. A **72**, 053604 (2005).
[57] A. B. Kuklov, Unconventional Strongly Interacting Bose-Einstein Condensates in Optical Lattices, Phys. Rev. Lett. **97**, 110405 (2006).
[58] W. V. Liu and C. Wu, Atomic matter of nonzero-momentum Bose-Einstein condensation and orbital current order, Phys. Rev. A **74**, 013607 (2006).
[59] T. Müller, S. Fölling, A. Widera, and I. Bloch, State Preparation and Dynamics of Ultracold Atoms in Higher Lattice Orbitals, Phys. Rev. Lett. **99**, 200405 (2007).
[60] G. Wirth, M. Olschlager, and A. Hemmerich, Evidence for orbital superfluidity in the p-band of a bipartite optical square lattice, Nat. Phys. **7**, 147 (2011).
[61] C. V. Parker, L.-C. Ha, and C. Chin, Direct observation of effective ferromagnetic domains of cold atoms in a shaken optical lattice, Nat. Phys. **9**, 769 (2013).
[62] M. A. Khamehchi, C. Qu, M. E. Mossman, C. Zhang, and P. Engels, Spin-momentum coupled Bose-Einstein condensates with lattice band pseudospins, Nat. Commun. **7**, 10867 (2016).
[63] J. H. Shirley, Solution of the Schrödinger equation with a Hamiltonian periodic in time, Phys. Rev. **138**, B979 (1965).
[64] H. Sambe, Steady states and quasienergies of a quantum-mechanical system in an oscillating field, Phys. Rev. A **7**, 2203 (1973).
[65] F. Gesztesy and H. Mitter, A note on quasi-periodic states, Journal of Physics A: Mathematical and General **14**, L79 (1981).
[66] W. Magnus, On the exponential solution of differential equations for a linear operator, Commun. Pure Appl. Math. **7**, 649 (1954).
[67] S. Blanes, F. Casas, J. Oteo, and J. Ros, The Magnus expansion and some of its applications, Phys. Rep. **470**, 151 (2009).
[68] E. Fel'dman, On the convergence of the Magnus expansion for spin systems in periodic magnetic fields, Phys. Lett. A **104**, 479 (1984).
[69] M. M. Maricq, Application of average Hamiltonian theory to the NMR of solids, Phys. Rev. B **25**, 6622 (1982).
[70] T. P. Grozdanov and M. J. Raković, Quantum system driven by rapidly varying periodic perturbation, Phys. Rev. A **38**, 1739 (1988).
[71] S. Rahav, I. Gilary, and S. Fishman, Effective Hamiltonians for periodically driven systems, Phys. Rev. A **68**, 013820 (2003).
[72] S. Rahav, I. Gilary, and S. Fishman, Time Independent Description of Rapidly Oscillating Potentials, Phys. Rev. Lett. **91**, 110404 (2003).
[73] N. Goldman and J. Dalibard, Periodically Driven Quantum Systems: Effective Hamiltonians and Engineered Gauge Fields, Phys. Rev. X **4**, 031027 (2014).
[74] A. Eckardt and E. Anisimovas, Consistent high-frequency approximation for periodically driven quantum systems, New. J. Phys. **17**, 093039 (2015).

[75] M. Bukov, L. D'Alessio, and A. Polkovnikov, Universal high-frequency behavior of periodically driven systems: from dynamical stabilization to Floquet engineering, Adv. Phys. **64**, 139 (2015).

[76] T. Prosen, Quantum invariants of motion in a generic many-body system, Journal of Physics A: Mathematical and General **31**, L645 (1998).

[77] T. Prosen, Time Evolution of a Quantum Many-Body System: Transition from Integrability to Ergodicity in the Thermodynamic Limit, Phys. Rev. Lett. **80**, 1808 (1998).

[78] T. Prosen, Ergodic properties of a generic nonintegrable quantum many-body system in the thermodynamic limit, Phys. Rev. E **60**, 3949 (1999).

[79] T. Prosen and E. Ilievski, Nonequilibrium Phase Transition in a Periodically Driven xy Spin Chain, Phys. Rev. Lett. **107**, 060403 (2011).

[80] L. D'Alessio and A. Polkovnikov, Many-body energy localization transition in periodically driven systems, Ann. Phys. **333**, 19 (2013).

[81] L. D'Alessio and M. Rigol, Long-Time Behavior of Isolated Periodically Driven Interacting Lattice Systems, Phys. Rev. X **4**, 041048 (2014).

[82] A. Lazarides, A. Das, and R. Moessner, Periodic Thermodynamics of Isolated Quantum Systems, Phys. Rev. Lett. **112**, 150401 (2014).

[83] A. Lazarides, A. Das, and R. Moessner, Fate of Many-Body Localization under Periodic Driving, Phys. Rev. Lett. **115**, 030402 (2015).

[84] P. Ponte, Z. Papić, F. Huveneers, and D. A. Abanin, Many-Body Localization in Periodically Driven Systems, Phys. Rev. Lett. **114**, 140401 (2015).

[85] D. A. Abanin, W. De Roeck, and F. Huveneers, Exponentially Slow Heating in Periodically Driven Many-Body Systems, Phys. Rev. Lett. **115**, 256803 (2015).

[86] D. Abanin, W. De Roeck, and W. Ho, Effective Hamiltonians, prethermalization and slow energy absorption in periodically driven many-body systems, arXiv:1510.03405.

[87] M. Genske and A. Rosch, Floquet-Boltzmann equation for periodically driven Fermi systems, Phys. Rev. A **92**, 062108 (2015).

[88] T. Mori, T. Kuwahara, and K. Saito, Rigorous Bound on Energy Absorption and Generic Relaxation in Periodically Driven Quantum Systems, Phys. Rev. Lett. **116**, 120401 (2016).

[89] T. Kuwahara, T. Mori, and K. Saito, Floquet-Magnus theory and generic transient dynamics in periodically driven many-body quantum systems, Ann. Phys. **367**, 96 (2016).

[90] A. Eckardt and M. Holthaus, Avoided-Level-Crossing Spectroscopy with Dressed Matter Waves, Phys. Rev. Lett. **101**, 245302 (2008).

[91] M. Heyl and S. Kehrein, Nonequilibrium steady state in a periodically driven Kondo model, Phys. Rev. B **81**, 144301 (2010).

[92] A. Russomanno, A. Silva, and G. E. Santoro, Periodic Steady Regime and Interference in a Periodically Driven Quantum System, Phys. Rev. Lett. **109**, 257201 (2012).

[93] R. Citro, E. G. D. Torre, L. D'Alessio, A. Polkovnikov, M. Babadi, T. Oka, and E. Demler, Dynamical stability of a many-body Kapitza pendulum, Ann. Phys. **360**, 694 (2015).

[94] T. Bilitewski and N. R. Cooper, Scattering theory for Floquet-Bloch states, Phys. Rev. A **91**, 033601 (2015).

[95] M. Bukov, M. Heyl, D. A. Huse, and A. Polkovnikov, Heating and many-body resonances in a periodically driven two-band system, Phys. Rev. B **93**, 155132 (2016).

[96] N. Goldman, J. Dalibard, M. Aidelsburger, and N. R. Cooper, Periodically driven quantum matter: The case of resonant modulations, Phys. Rev. A **91**, 033632 (2015).

[97] T. Oka and H. Aoki, Photovoltaic Hall effect in graphene, Phys. Rev. B **79**, 081406 (2009).

[98] H. L. Calvo, H. M. Pastawski, S. Roche, and L. E. F. F. Torres, Tuning laser-induced band gaps in graphene, Appl. Phys. Lett. **98**, 232103 (2011).

[99] T. Kitagawa, T. Oka, A. Brataas, L. Fu, and E. Demler, Transport properties of nonequilibrium systems under the application of light: Photoinduced quantum Hall insulators without Landau levels, Phys. Rev. B **84**, 235108 (2011).

[100] E. Suárez Morell and L. E. F. Foa Torres, Radiation effects on the electronic properties of bilayer graphene, Phys. Rev. B **86**, 125449 (2012).

[101] N. H. Lindner, G. Refael, and V. Galitski, Floquet topological insulator in semiconductor quantum wells, Nat. Phys. **7**, 490 (2011).

[102] N. H. Lindner, D. L. Bergman, G. Refael, and V. Galitski, Topological Floquet spectrum in three dimensions via a two-photon resonance, Phys. Rev. B **87**, 235131 (2013).

[103] J. Cayssol, B. Dóra, F. Simon, and R. Moessner, Floquet topological insulators, Physica Status Solidi (RRL)–Rapid Research Letters **7**, 101 (2013).

[104] P. Delplace, A. Gómez-León, and G. Platero, Merging of Dirac points and Floquet topological transitions in ac-driven graphene, Phys. Rev. B **88**, 245422 (2013).

[105] A. G. Grushin, A. Gómez-León, and T. Neupert, Floquet Fractional Chern Insulators, Phys. Rev. Lett. **112**, 156801 (2014).

[106] A. Gómez-León, P. Delplace, and G. Platero, Engineering anomalous quantum Hall plateaus and antichiral states with ac fields, Phys. Rev. B **89**, 205408 (2014).

[107] Y. H. Wang, H. Steinberg, P. Jarillo-Herrero, and N. Gedik, Observation of Floquet-Bloch states on the surface of a topological insulator, Science **342**, 453 (2013).

[108] L. Jiang, T. Kitagawa, J. Alicea, A. R. Akhmerov, D. Pekker, G. Refael, J. I. Cirac, E. Demler, M. D. Lukin, and P. Zoller, Majorana Fermions in Equilibrium and in Driven Cold-Atom Quantum Wires, Phys. Rev. Lett. **106**, 220402 (2011).

[109] G. Liu, N. Hao, S.-L. Zhu, and W. M. Liu, Topological superfluid transition induced by a periodically driven optical lattice, Phys. Rev. A **86**, 013639 (2012).

[110] Q.-J. Tong, J.-H. An, J. Gong, H.-G. Luo, and C. H. Oh, Generating many Majorana modes via periodic driving: A superconductor model, Phys. Rev. B **87**, 201109 (2013).

[111] M. Thakurathi, A. A. Patel, D. Sen, and A. Dutta, Floquet generation of Majorana end modes and topological invariants, Phys. Rev. B **88**, 155133 (2013).

[112] A. Kundu and B. Seradjeh, Transport Signatures of Floquet Majorana Fermions in Driven Topological Superconductors, Phys. Rev. Lett. **111**, 136402 (2013).

[113] Z. bo Wang, H. Jiang, H. Liu, and X. Xie, Floquet Majorana fermions in driven hexagonal lattice systems, Solid State Commun. **215-216**, 18 (2015).

[114] T. Kitagawa, E. Berg, M. Rudner, and E. Demler, Topological characterization of periodically driven quantum systems, Phys. Rev. B **82**, 235114 (2010).

[115] M. S. Rudner, N. H. Lindner, E. Berg, and M. Levin, Anomalous Edge States and the Bulk-Edge Correspondence for Periodically Driven Two-Dimensional Systems, Phys. Rev. X **3**, 031005 (2013).

[116] A. Gómez-León and G. Platero, Floquet-Bloch Theory and Topology in Periodically Driven Lattices, Phys. Rev. Lett. **110**, 200403 (2013).

[117] M. Lababidi, I. I. Satija, and E. Zhao, Counter-Propagating Edge Modes and Topological Phases of a Kicked Quantum Hall System, Phys. Rev. Lett. **112**, 026805 (2014).

[118] P. M. Perez-Piskunow, G. Usaj, C. A. Balseiro, and L. E. F. Foa Torres, Floquet chiral edge states in graphene, Phys. Rev. B **89**, 121401 (2014).

[119] D. Carpentier, P. Delplace, M. Fruchart, and K. Gawedzki, Topological Index for Periodically Driven Time-Reversal Invariant 2D Systems, Phys. Rev. Lett. **114**, 106806 (2015).

[120] F. Nathan and M. S. Rudner, Topological singularities and the general classification of Floquet-Bloch systems, New J. Phys. **17**, 125014 (2015).

[121] A. C. Potter, T. Morimoto, and A. Vishwanath, Topological classification of interacting Floquet phases in one dimension, Phys. Rev. X **6**, 041001 (2016).

[122] L. J. Maczewsky, J. M. Zeuner, S. Nolte, and A. Szameit, Observation of photonic anomalous Floquet topological insulators, arXiv:1605.03877.

[123] A. Kitaev, Periodic table for topological insulators and superconductors, AIP Conf. Proc. **1134**, 22 (2009).

[124] K. Fang, Z. Yu, and S. Fan, Realizing effective magnetic field for photons by controlling the phase of dynamic modulation, Nat. Photon. **6**, 782 (2012).

[125] K. Fang, Z. Yu, and S. Fan, Photonic de Haas-van Alphen effect, Opt. Express **21**, 18216 (2013).

[126] P. Roushan, C. Neill, A. Megrant, Y. Chen, R. Babbush, R. Barends, B. Campbell, Z. Chen, B. Chiaro, A. Dunsworth, A. Fowler, E. Jeffrey, J. Kelly, E. Lucero, J. Mutus, P. J. J. O'Malley, M. Neeley, C. Quintana, D. Sank, A. Vainsencher, J. Wenner, T. White, E. Kapit, H. Neven, and J. Martinis, Chiral ground-state currents of interacting photons in a synthetic magnetic field, Nat. Phys. (2016).

[127] F. D. M. Haldane, Effective Harmonic-Fluid Approach to Low-Energy Properties of One-Dimensional Quantum Fluids, Phys. Rev. Lett. **47**, 1840 (1981).

[128] A. Gogolin, A. Nersesyan, and A. Tsvelik, *Bosonization and Strongly Correlated Systems* (Cambridge University Press, Cambridge, 2004).

[129] T. Giamarchi, *Quantum Physics in One Dimension*, International Series of Monographs on Physics (Clarendon Press, Oxford, 2003).

[130] M. A. Cazalilla, R. Citro, T. Giamarchi, E. Orignac, and M. Rigol, One-dimensional bosons: From condensed matter systems to ultracold gases, Rev. Mod. Phys. **83**, 1405 (2011).

[131] A. L. C. Hayward, A. M. Martin, and A. D. Greentree, Fractional Quantum Hall Physics in Jaynes-Cummings-Hubbard Lattices, Phys. Rev. Lett. **108**, 223602 (2012).

[132] J. Koch, A. A. Houck, K. L. Hur, and S. M. Girvin, Time-reversal-symmetry breaking in circuit-QED-based photon lattices, Phys. Rev. A **82**, 043811 (2010).

[133] W. Zheng and H. Zhai, Floquet topological states in shaking optical lattices, Phys. Rev. A **89**, 061603 (2014).

[134] A. R. Kolovsky, Creating artificial magnetic fields for cold atoms by photon-assisted tunneling, Europhys. Lett. **93**, 20003 (2011).

[135] M. Boissonneault, J. M. Gambetta, and A. Blais, Dispersive regime of circuit QED: Photon-dependent qubit dephasing and relaxation rates, Phys. Rev. A **79**, 013819 (2009).

[136] A. J. Hoffman, S. J. Srinivasan, S. Schmidt, L. Spietz, J. Aumentado, H. E. Türeci, and A. A. Houck, Dispersive Photon Blockade in a Superconducting Circuit, Phys. Rev. Lett. **107**, 053602 (2011).

[137] F. J. Dyson, The s matrix in quantum electrodynamics, Phys. Rev. **75**, 1736 (1949).

[138] G. W. Semenoff, Condensed-Matter Simulation of a Three-Dimensional Anomaly, Phys. Rev. Lett. **53**, 2449 (1984).

[139] A. Petrescu, A. A. Houck, and K. Le Hur, Anomalous Hall effects of light and chiral edge modes on the kagome lattice, Phys. Rev. A **86**, 053804 (2012).

[140] T. Liu, B. Douçot, and K. Le Hur, Anisotropic quantum spin Hall effect, spin-orbital textures, and the Mott transition, Phys. Rev. B **88**, 245119 (2013).

[141] J. Colpa, Diagonalization of the quadratic boson Hamiltonian, Physica A **93**, 327 (1978).

[142] S. Furukawa and M. Ueda, Excitation band topology and edge matter waves in Bose-Einstein condensates in optical lattices, New J. Phys. **17**, 115014 (2015).

[143] C. L. Henley, Ordering due to Disorder in a Frustrated Vector Antiferromagnet, Phys. Rev. Lett. **62**, 2056 (1989).

[144] Y. Kuno, T. Nakafuji, and I. Ichinose, Phase diagrams of the Bose-Hubbard model and the Haldane-Bose-Hubbard model with complex hopping amplitudes, Phys. Rev. A **92**, 063630 (2015).

[145] E. Orignac and T. Giamarchi, Meissner effect in a bosonic ladder, Phys. Rev. B **64**, 144515 (2001).

[146] A. Dhar, M. Maji, T. Mishra, R. V. Pai, S. Mukerjee, and A. Paramekanti, Bose-Hubbard model in a strong effective magnetic field: Emergence of a chiral Mott insulator ground state, Phys. Rev. A **85**, 041602 (2012).

[147] A. Petrescu and K. Le Hur, Bosonic Mott Insulator with Meissner Currents, Phys. Rev. Lett. **111**, 150601 (2013).

[148] A. Tokuno and A. Georges, Ground states of a Bose-Hubbard ladder in an artificial magnetic field: field-theoretical approach, New J. Phys. **16**, 073005 (2014).

[149] M. Piraud, F. Heidrich-Meisner, I. P. McCulloch, S. Greschner, T. Vekua, and U. Schollwöck, Vortex and Meissner phases of strongly interacting bosons on a two-leg ladder, Phys. Rev. B **91**, 140406 (2015).

[150] S. Greschner, M. Piraud, F. Heidrich-Meisner, I. P. McCulloch, U. Schollwöck, and T. Vekua, Spontaneous Increase of Magnetic Flux and Chiral-Current Reversal in Bosonic Ladders: Swimming Against the Tide, Phys. Rev. Lett. **115**, 190402 (2015).

[151] A. Keleş and M. O. Oktel, Mott transition in a two-leg Bose-Hubbard ladder under an artificial magnetic field, Phys. Rev. A **91**, 013629 (2015).

[152] E. Orignac, R. Citro, M. D. Dio, S. D. Palo, and M.-L. Chiofalo, Incommensurate phases of a bosonic two-leg ladder under a flux, New J. Phys. **18**, 055017 (2016).

[153] A. Petrescu and K. Le Hur, Chiral Mott insulators, Meissner effect, and Laughlin states in quantum ladders, Phys. Rev. B **91**, 054520 (2015).

[154] M. Mancini, G. Pagano, G. Cappellini, L. Livi, M. Rider, J. Catani, C. Sias, P. Zoller, M. Inguscio, M. Dalmonte, and L. Fallani, Observation of chiral edge states with neutral fermions in synthetic hall ribbons, Science **349**, 1510 (2015).

[155] B. K. Stuhl, H.-I. Lu, L. M. Aycock, D. Genkina, and I. B. Spielman, Visualizing edge states with an atomic Bose gas in the quantum Hall regime, Science **349**, 1514 (2015).

[156] M. Lacki, H. Pichler, A. Sterdyniak, A. Lyras, V. E. Lembessis, O. Al-Dossary, J. C. Budich, and P. Zoller, Quantum Hall physics with cold atoms in cylindrical optical lattices, Phys. Rev. A **93**, 013604 (2016).

[157] S. Barbarino, L. Taddia, D. Rossini, L. Mazza, and R. Fazio, Synthetic gauge fields in synthetic dimensions: interactions and chiral edge modes, New J. Phys. **18**, 035010 (2016).

[158] L. Taddia, E. Cornfeld, D. Rossini, L. Mazza, E. Sela, and R. Fazio, Topological fractional pumping with alkaline-earth(-like) ultracold atoms, arXiv:1607.07842.

[159] J. Klinovaja, P. Stano, and D. Loss, Topological Floquet Phases in Driven Coupled Rashba Nanowires, Phys. Rev. Lett. **116**, 176401 (2016).

[160] D. Hügel and B. Paredes, Chiral ladders and the edges of quantum Hall insulators, Phys. Rev. A **89**, 023619 (2014).

[161] D. Sticlet, L. Seabra, F. Pollmann, and J. Cayssol, From fractionally charged solitons to Majorana bound states in a one-dimensional interacting model, Phys. Rev. B **89**, 115430 (2014).

[162] S. Rachel and K. Le Hur, Topological insulators and Mott physics from the Hubbard interaction, Phys. Rev. B **82**, 075106 (2010).

[163] T. Liu, C. Repellin, B. Douçot, N. Regnault, and K. Le Hur, Triplet FFLO superconductivity in the doped Kitaev-Heisenberg honeycomb model, Phys. Rev. B **94**, 180506 (2016).